Development and Implementation of Automatic Modal Identification

BSEE Project Report

Contract Number 140E0119C0003

Mingming Song, Babak Moaveni, Eric Hines

Dept. of Civil and Environmental Engineering, Tufts University, Medford, MA

August 2021

Contents

1. Summary

This report provides the details of developed automated approach for data processing and modal identification of the instrumented wind turbine (B2) at the Block Island Wind Farm. We have developed and implemented an automated system identification approach for extracting modal parameters of B2 wind turbine using the measured wired accelerations through the continuous monitoring system. The data-driven stochastic subspace identification (SSI-DATA) [1, 2] method is automated and implemented for identification of modal parameters.

Following an introduction to modal identification, the report reviews the monitoring system and the collected measurements for modal/system identification in Section 3. Data cleansing and the automated system identification method are detailed in Section 4. Section 5 provides analysis of obtained results for different periods of time, including (1) three cases of a full day analysis with constant rotor speed, rapidly varying rotor speed, and parked turbine; (2) two cases of a full week analysis, one is from 4/21 to 4/27 when turbine is in operation, and the other one is from 7/5 to 7/11 when turbine is parked; (3) an overview analysis over a 3-month period from April 19 to July 19. Finally, Section 6 presents the conclusions made from the observations.

2. Introduction

Modal parameters include natural frequencies, mode shapes and damping ratios which represent dynamic characteristics of structures. Modal parameters are informative structural signatures which are useful for condition assessment and response prediction [3]. In the recent years, modal parameters haven been extensively used for structural assessment and response prediction. Model updating is one of the most common methods for the purpose of structural heath monitoring, and many applications of model updating have used modal parameters as data features to calibrate the numerical model and estimate uncertain parameters of the model [4-13].

Modal parameters can be identified using various types of dynamic measurements such as acceleration, velocity, strain, or displacement. Numerous system identification methods have been developed in the literature over the last few decades, including peak-picking [14], ARX method [2], general realization algorithm (GRA) [15], eigensystem realization algorithm (ERA) [16], ERA combined with the natural excitation technique (NExT-ERA) [17], frequency domain decomposition (FDD) [18], covariance-driven stochastic subspace identification (SSI-COV), and data-driven stochastic subspace identification (SSI-DATA) [1, 19].

These methods can be classified into different categories based on different criteria. Based on whether the input information is available or measured, these methods can be grouped into input-output or output-only. If both the input excitation force and output response are measured and used for modal identification then the method is an input-output method, while output-only methods only use the output response. For the output-only case, the unknown excitation is usually assumed to have certain statistical properties, for instance, broadband white noise excitation. System identification methods are also categorized into non-parametric versus parametric methods. In non-parametric methods, no model is fit to the measured data such as the peak-picking method in which natural frequencies are estimated as peaks of the measured

frequency response function. In parametric methods, a mathematical model is first fit to the data and then modal parameters are estimated from the model. Alternatively, system identification methods can be grouped based on the type of data used. Some methods work with the data in frequency-domain, for instance, FDD, while other methods directly use time history data, for instance, SSI-DATA. SSI-DATA is an output-only, parametric, and time-domain system identification method and is formulated and automated [20] for application in this project. SSI-DATA has been shown to provide accurate and unbiased results and is flexible for automation.

3. Continuous Monitoring System of BIWF

The BIWF is the first commercial offshore wind farm in the US, and is located 3.8 miles from Block Island, Rode Island in the Atlantic Ocean. It is operated by Ørsted and consists of 5 Alstom Haliade 6 MW turbines manufactured by General Electric (GE), and therefore, has a total capacity of 30 MW. The five wind turbines are named as 'B1', 'B2', 'B3', B4' and 'B5', and the continuous monitoring system was instrumented on wind turbine 'B2'. The BIWF and B2 wind turbine are shown in Figure 1.

(a)

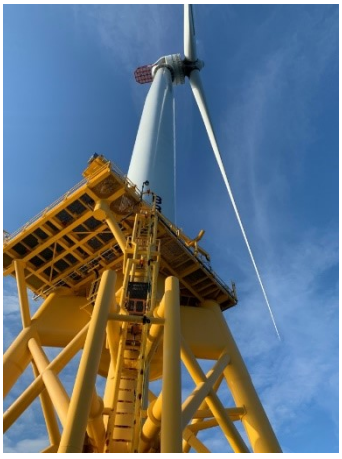

(b)

Figure 1. (a) BIWF (by Eric Thayer/Bloomberg); (b) B2 wind turbine.

The continuous monitoring system currently consists of 9 wired accelerometers, 4 wireless accelerometers and 2 inclinometers. The complete monitoring system will also include 8 full bridge strain gauges which will be mounted 0.5 m above the flange connection to the transition piece. The installation of strain gauges is expected to happen later this year. The instrumentation system, including sensors, cables, and data acquisition system, are designed and provided by the Norwegian Geotechnical Institute (NGI). DEWESoft-X3 software is installed on the data acquisition CPU for system configuration, real-time analysis and data export/storage. The wired accelerometers are named as 'A1' to 'A10', but A8 was not installed currently due to the shortage of cables. A7, A8 and A10 are biaxial accelerometers, and the others are triaxial. The type of triaxial accelerometers is MonoDAQ-E-gMeter which is fully integrated low-noise 3D MEMS accelerometer, and the bi-axial accelerometers are assembled using 2 PCB 393B04 ICP accelerometers mounted inside a waterproof enclosure. 4 wireless triaxial accelerometers are equipped with a gateway and batteries with a capacity of about 1-month continuous recording.

The installed inclinometers are temperature compensated biaxial MEMS inclinometers and mounted inside the DAQ cabinet. The wireless accelerometers are not currently collecting data, probably due to the obstruction between the accelerometers and their gateway transceiver. A total of 9 accelerometers and 2 inclinometers are working properly and providing high-quality measurements continuously since April 18, 2021. The monitoring system has a sampling frequency of 50 Hz and stores 10 min measurements into a series of datasets. The accelerometers and the data acquisition system are shown in Figure 2. The layout of accelerometers is shown in Figure 3. The horizontal measurement directions of the accelerometers ($\overline{X}$ and $\overline{Y}$) are rotated 45° clockwise from the global coordinate system (X and Y).

(a) (b)

Figure 2. Data acquisition system (a) and accelerometers (b).

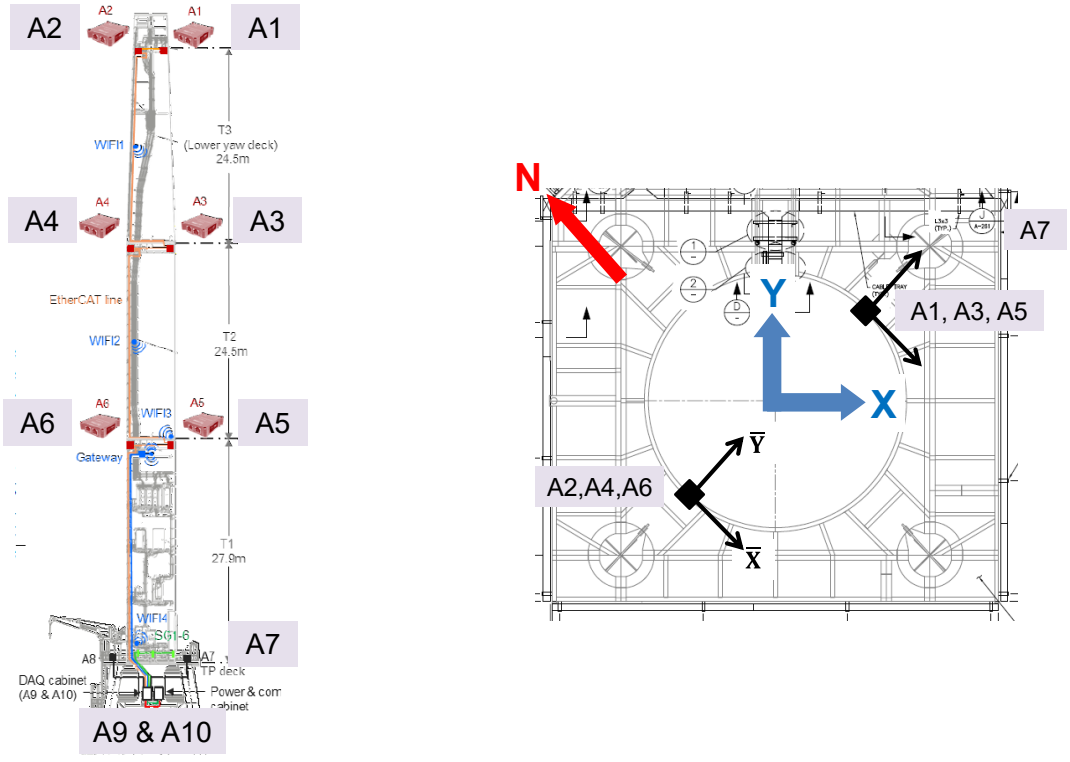

(a) (b)

Figure 3. Elevation (a) and top view (b) of accelerometers instrumentation.

4. Data Cleansing and Automated System Identification

This section presents the data pre-processing and a concise framework of SSI-DATA for automated system identification using pre-processed time history measurements [1, 20].

4.1 Data cleansing

The measurements of B2 turbine are pre-processed and cleaned before they are fed into the SSI-DATA algorithm introduced in next section for extracting modal parameters. In the first of data cleansing, the spikes in the raw measurements are removed and replaced with interpolated values. The spikes are defined as any samples whose values are larger than 8 times the standard deviation of the signals. Then the cleaned signals are filtered between 0.1 and 3.2 Hz in frequency domain to focus on the frequency band of interest and remove the effect of high-frequency noise. The frequency band is selected to include the first few most important modes of the structure. The signals are finally down-sampled from 50 Hz to 8 Hz to improve the computation efficiency.

4.2 SSI-DATA method

Consider the following stochastic dynamic system in state-space formulation:

$$\begin{aligned} \mathbf{x}_{k+1} &= \mathbf{A}\mathbf{x}_k + \mathbf{w}_k \\ \mathbf{y}_k &= \mathbf{C}\mathbf{x}_k + \mathbf{v}_k \end{aligned} \tag{1}$$

The SSI-DATA method provides an estimate for the state-space and output matrices (**A** and **C**) of a linear dynamic system, and then the modal parameters of the system are estimated from these matrices.

In the application of SSI-DATA, a Hankel matrix is created from measured time history data. The matrix is divided into two parts: 'past' Hankel matrix $\mathbf{H}_p$ and 'future' Hankel matrix $\mathbf{H}_f$ which are defined as:

$$\mathbf{H}_p = \frac{1}{\sqrt{\beta}} \begin{bmatrix} \mathbf{y}_0^{ref} & \mathbf{y}_1^{ref} & \cdots & \mathbf{y}_{\beta-1}^{ref} \\ \mathbf{y}_1^{ref} & \mathbf{y}_2^{ref} & \cdots & \mathbf{y}_{\beta}^{ref} \\ \vdots & \vdots & \ddots & \vdots \\ \mathbf{y}_{\alpha-1}^{ref} & \mathbf{y}_{\alpha}^{ref} & \cdots & \mathbf{y}_{\alpha+\beta-2}^{ref} \end{bmatrix} \tag{2}$$

$$\mathbf{H}_f = \frac{1}{\sqrt{\beta}} \begin{bmatrix} \mathbf{y}_{\alpha} & \mathbf{y}_{\alpha+1} & \cdots & \mathbf{y}_{\alpha+\beta-1} \\ \mathbf{y}_{\alpha+1} & \mathbf{y}_{\alpha+2} & \cdots & \mathbf{y}_{\alpha+\beta} \\ \vdots & \vdots & \ddots & \vdots \\ \mathbf{y}_{2\alpha-1} & \mathbf{y}_{2\alpha} & \cdots & \mathbf{y}_{2\alpha+\beta-2} \end{bmatrix} \tag{3}$$

$$\mathbf{H} = \begin{bmatrix} \mathbf{H}_p \\ \mathbf{H}_f \end{bmatrix} \tag{4}$$

The information in $\mathbf{H}_p$ will be used to predict $\mathbf{H}_f$. The least square error solution of the predicted 'future' Hankel matrix is [1]:

$$\mathbf{H}_f \approx \mathbf{L}\mathbf{H}_p = \mathbf{H}_f\mathbf{H}_p^T\left(\mathbf{H}_p\mathbf{H}_p^T\right)^+\mathbf{H}_p \tag{5}$$

where the symbol '+' denotes pseudo-inverse operation. This predicted 'future' Hankel matrix can be seen as the orthogonal projection of the row space of $\mathbf{H}_f$ into the row space of $\mathbf{H}_p$, and is denoted as $\mathbf{P}_\alpha$. This projection can be factorized as the product of an observability matrix $\mathbf{P}_\alpha$ and a sequence of Kalman filter state estimates $\hat{\mathbf{X}}_\alpha$:

$$\mathbf{P}_\alpha = \mathbf{P}_\alpha\hat{\mathbf{X}}_\alpha \tag{6}$$

The projection can be computed directly using Eq. (5), but it is often evaluated using QR factorization. After that, the projection is factored using singular value decomposition (SVD):

$$\mathbf{P}_\alpha = \mathbf{U}\mathbf{\Sigma}_v\mathbf{V}^T \tag{7}$$

Then a truncation can be made by retaining the *n* largest singular values and excluding the rest to provide an approximate solution of the observability matrix and the state estimates:

$$\mathbf{P}_\alpha = \mathbf{U}_n\mathbf{\Sigma}_n^{1/2}, \quad \hat{\mathbf{X}}_\alpha = \mathbf{\Sigma}_n^{1/2}\mathbf{V}_n^T \tag{8}$$

Next, the division between 'past' and 'future' Hankel matrices is shifted one block row downwards, and then $\mathbf{H}_f^-$ and $\mathbf{H}_p^+$ are created. The shifted projection $\mathbf{P}_{\alpha-1}$ is computed and factored in the same way:

$$\mathbf{P}_{\alpha-1} = \mathbf{P}_{\alpha-1}\hat{\mathbf{X}}_{\alpha+1} \tag{9}$$

Then the shifted Kalman filter sequence can be determined by:

$$\hat{\mathbf{X}}_{\alpha+1} = \mathbf{P}_{\alpha-1}^+\mathbf{P}_{\alpha-1} \tag{10}$$

A sequence $\mathbf{Y}_{\alpha|\alpha}$ is defined as the measured output sequence at the same time steps of $\hat{\mathbf{X}}_\alpha$:

$$\mathbf{Y}_{\alpha|\alpha} = \begin{bmatrix} \mathbf{y}_\alpha & \mathbf{y}_{\alpha+1} & \cdots & \mathbf{y}_{\alpha+\beta-1} \end{bmatrix} \tag{11}$$

The state-space matrices of the system in discrete-time can be computed as:

$$\begin{bmatrix} \hat{\mathbf{A}} \\ \hat{\mathbf{C}} \end{bmatrix} = \begin{bmatrix} \hat{\mathbf{X}}_{\alpha+1} \\ \mathbf{Y}_{\alpha|\alpha} \end{bmatrix}\hat{\mathbf{X}}_{\alpha+1}^+ \tag{12}$$

To obtain the modal parameters from the estimated state matrices, an eigenvalue analysis is first performed on matrix $\hat{\mathbf{A}}$:

$$\mathbf{\Lambda} = \mathbf{\Psi}^{-1}\hat{\mathbf{A}}\mathbf{\Psi} \tag{13}$$

in which $\mathbf{\Lambda}$ denotes matrix of eigenvalues, and $\mathbf{\Psi}$ is matrix of eigenvectors. The continuous-time system matrix $\hat{\mathbf{A}}_c$ has the same eigenvectors as $\mathbf{\Psi}$, but its eigenvalues are:

$$\mathbf{\Lambda}_c = \frac{\ln(\mathbf{\Lambda})}{\Delta t} \tag{14}$$

where Δt denotes the sampling interval in time. The natural frequencies and damping ratios can be computed as:

$$\omega_i = \left|\lambda_{c,2i-1}\right| \tag{15}$$

$$\xi_i = -\frac{\text{Real}(\lambda_{c,2i-1})}{\omega_i} \tag{16}$$

where $\lambda_{c,2i-1}$ denotes the diagonal components of eigenvalue matrix $\mathbf{\Lambda}_c$. Note these eigenvalues are complex conjugate pairs, and alternating eigenvalues are used to compute modal parameters. The mode shapes are computed as:

$$\mathbf{\Phi} = \hat{\mathbf{C}}\mathbf{\Psi} \tag{17}$$

4.3 Automated system identification procedure

In the application of SSI-DATA for system identification, the system order (dimension of state matrix **A**) must be selected to fit a specific order of state space model to the measured data. If the measurement noise is zero and the system is observable, the system order can be simply determined as the number of nonzero singular values. However, for real-world applications, due to measurement noise and modeling errors, the division between significant and insignificant singular values is usually not obvious. For the SSI-DATA method, if the selected system order is too small, then some vibration modes of interest may be missed. If the order is too high, then spurious modes will be included in the identified modal parameters. Therefore, a stabilization diagram is often utilized to select the appropriate order for the system and to detect the stable modes of interest. Stabilization diagram shows the evolution of modal parameters over different system orders, where physical modes are expected to have stable or similar modal parameters for different orders. Some limits or criteria can be chosen to judge if a mode is stable or not. The system order can be selected so the number of observable modes of interest is maximized, or alternatively, stable modes can be estimated using different orders for different modes. Modes which are not stable are treated as spurious modes and are excluded from modal identification results.

The automated system identification algorithm in this project is based on the following automation procedure: at each system order, the identified modes are compared with their counterparts at pervious order. If the difference of frequencies and damping ratios between current system order and previous order is less than a pre-selected threshold and the modal assurance criterion (MAC) value is larger than or equal to a criterion value, then this mode is judged to be ‘stable’. The modal assurance criterion (MAC) between two vectors or mode shapes is defined as:

$$MAC_{i,j} = \frac{\left\|\boldsymbol{\varphi}_i^T \boldsymbol{\varphi}_j\right\|^2}{\left\|\boldsymbol{\varphi}_i\right\|^2 \left\|\boldsymbol{\varphi}_j\right\|^2} \tag{18}$$

The MAC value is a real number between 0 and 1, with values closer to 1 means better match between two mode shapes. If a mode remains stable consecutively for a specified number of

system orders, then it is assumed to be a physical mode of the structure. Modes with unrealistic damping ratios, for example, less than zero or larger than a threshold, will be excluded. Then the smallest order which provides a maximum number of physical modes of interest is selected as the best order of the state space model.

The criteria for 'stable' modes based on stabilization diagram in this application are set as: the relative difference of frequencies is less than 2%, relative change in damping ratios is less than 0.5, and the MAC values are larger than 0.9. Modes with damping ratios less than zero or larger than 15% are judged to spurious and are excluded. If a mode remains stable for 3 orders consecutively, it is assumed to be physical mode of the structure.

5. Results

5.1 Initial study of measurements in time and frequency domains

Samples of acceleration and inclination angle time histories measured at 9:17 on April 22, 2021 are shown in Figure 4 and Figure 5, respectively. Their Fourier amplitude spectra (FAS) are plotted in Figure 6 and Figure 7. From Figure 6, it is observed that the most significant peak is located at around 0.3 Hz which represents the first bending modes in fore-aft (FA) and side-to-side (SS) directions of the wind turbine. The 3P and 6P peaks are also evident which are caused by the rotor rotation and have frequencies at 3 times (3P) and 6 times (6P) of the revolution frequency of the rotor. Based on the specification of the wind turbine, the rotor has a speed range of 4 to 11.5 rpm, which represents a 1P frequency range of 0.067 to 0.192 Hz. Therefore, the 3P and 6P have ranges of 0.2 – 0.575 Hz, and 0.4 – 1.15 Hz, respectively. It is worth noting that 1P, unlike 3P and 6P, is hardly noticeable in the FAS plots of acceleration measurements. The sample FAS of acceleration data at 8:41 on July 9 are shown in Figure 8. The tropical storm Elsa was going through the area of BIWF on July 9, and the turbine was turned off and parked during this storm. It is observed that the second bending modes (2^{nd} SS/FA) are evident in the FAS plot which are located around 2.0 Hz (2^{nd} SS) and 2.3 Hz (2^{nd} FA). However, only one peak at 2.3 Hz is present on April 22 when the turbine is in operation. Based on the system identification results presented in following sections, the 2^{nd} FA/SS modes cannot be identified reliably using the data when the turbine is in operation but were identified with reasonable accuracy at parked condition. The possible reason is that the 12P, as well as the second flapwise and edgewise modes of the blades have frequency close to the 2^{nd} SS/FA modes, which causes modal interference and affects the system identification accuracy. The automatic system identification of the B2 wind turbine will be focused on the 1^{st} FA/SS modes when the turbine is in operation, and both 1^{st} and 2^{nd} FA/SS modes at parked condition. The results under different scenarios are presented in following sections in detail.

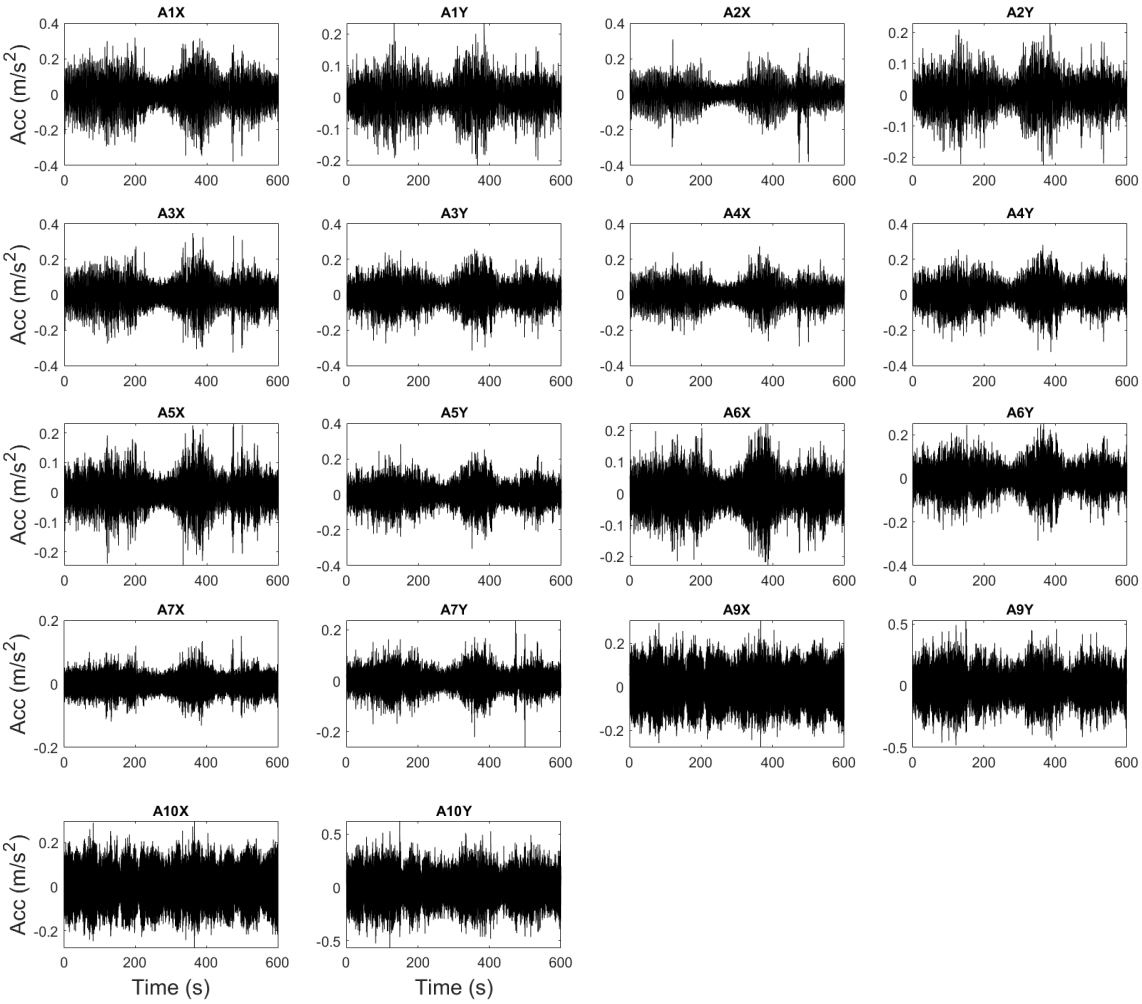

Figure 4. Sample of acceleration time histories at 9:17 on April 22.

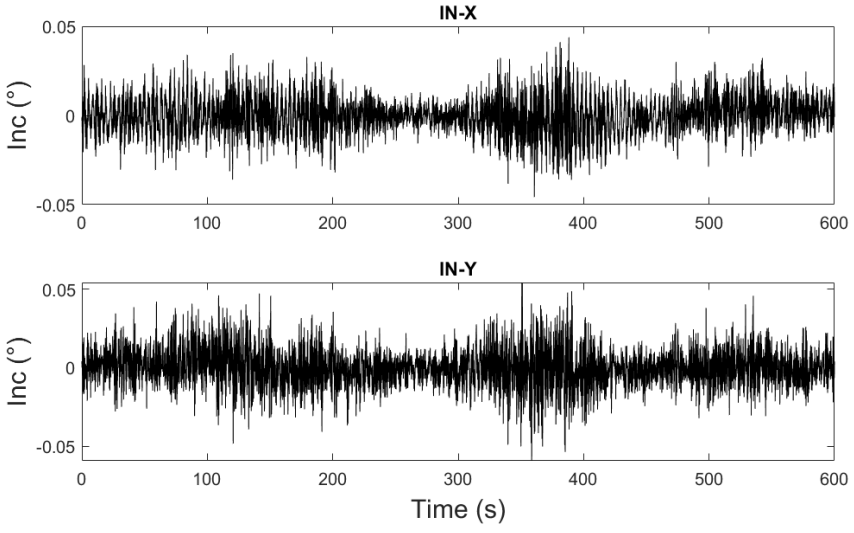

Figure 5. Sample of inclination time histories at 9:17 on April 22.

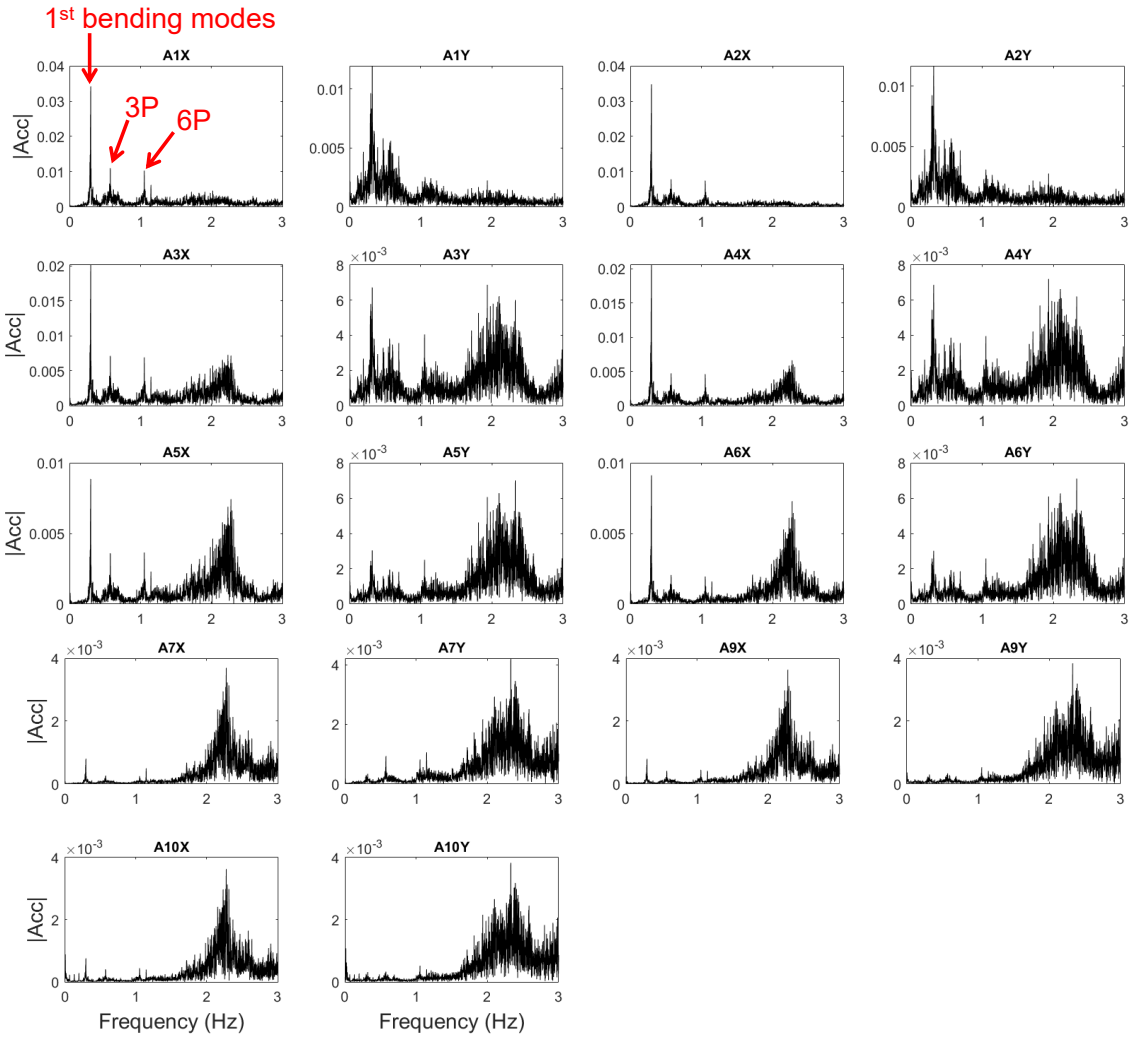

Figure 6. Sample of FAS of acceleration at 9:17 on April 22.

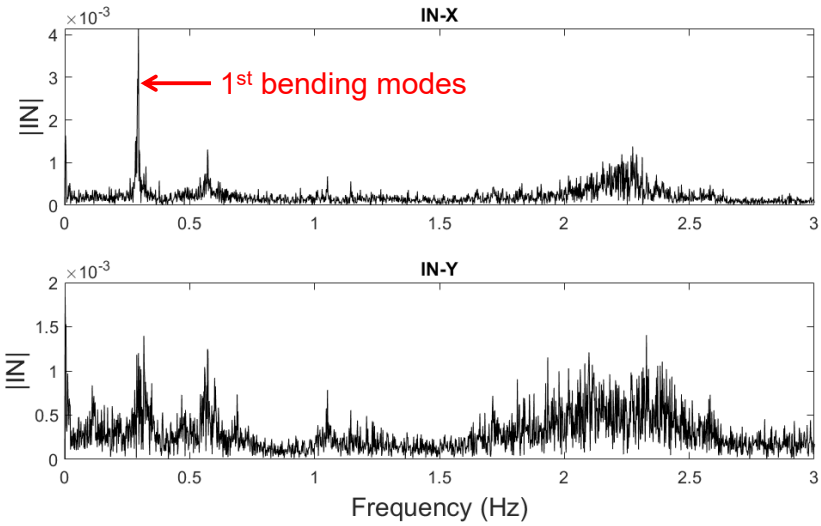

Figure 7. Sample of FAS of inclination at 9:17 on April 22.

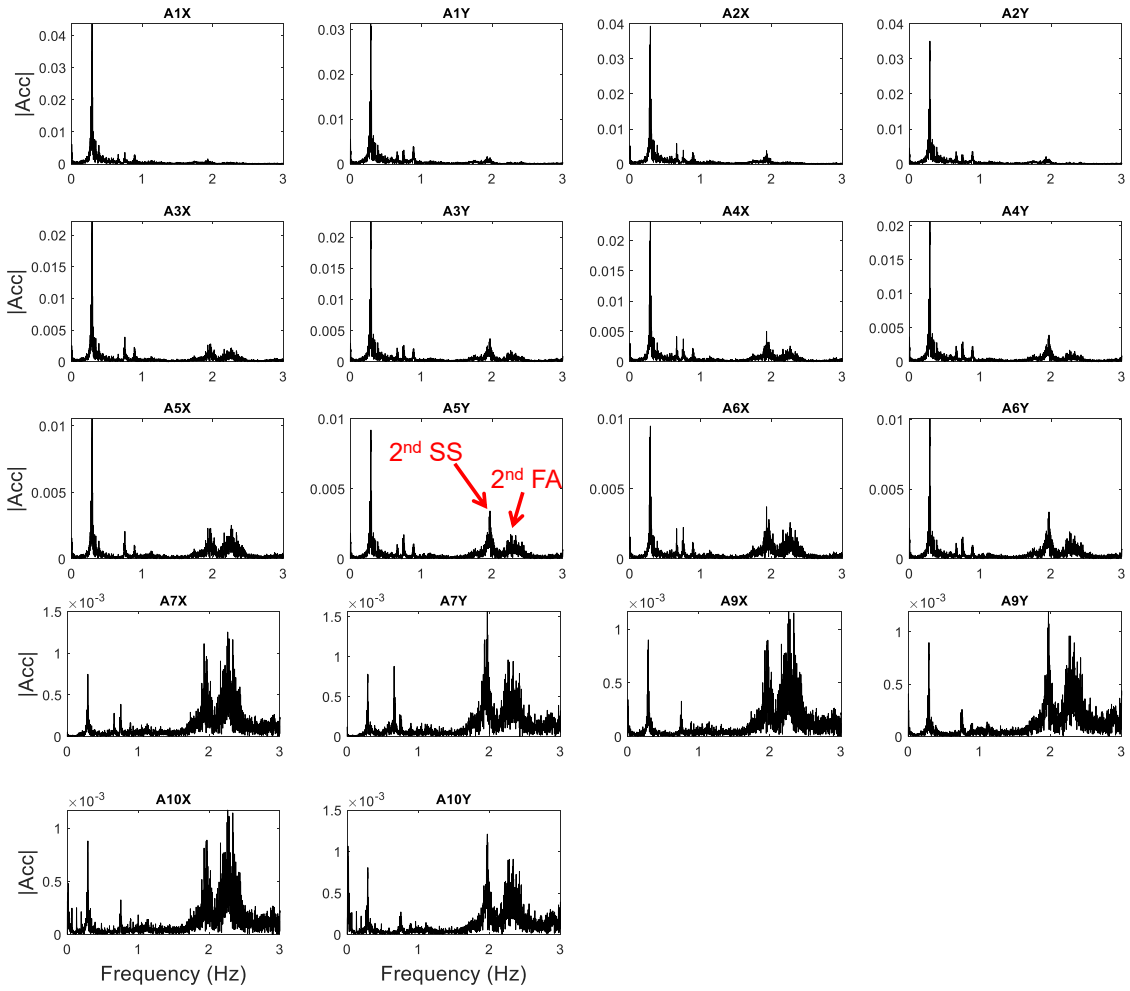

Figure 8. Sample of FAS of acceleration at 8:41 on July 9.

5.2 System identification over a day with constant rotor speed (April 22)

5.2.1 System identification results in global coordinates

The frequency stabilization diagram using the dataset at 9:17 on April 22 is shown in Figure 9. The circles present potential modes, and starred circles refer to modes which satisfy the stability criterion for frequency, i.e., the relative difference of frequencies between successive orders is less than 2%. The horizontal green line denotes the final order of the state space model which is selected based on the aforementioned automation procedure. Note that the vertical ordinate here shows the number of modes, which is equal to half of the model order in state-space. The logarithm of averaged power spectral density (PSD) over all channels is also plotted in Figure 9. It is observed that two closely-spaced modes are identified at around 0.3 Hz, which represent the FA and SS modes. In addition, 3P and 6P are also evident in the stabilization diagram. The mode shapes of SS and FA modes are shown in Figure 10 and Figure 11, respectively. Their compass plots representing the complex valued mode shapes (real vs. imaginary) are shown in Figure 12. It is seen that the large components of FA and SS modes are almost collinear in complex plane, meaning that they are almost classically damped. The system

identification results over the full day of April 22 are shown in Figure 13, where the 1P, 2P, 3P 6P, 9P, and 12P which are obtained from the supervisory control and data acquisition (SCADA) are also superposed in the plot. The wind speed on April 22 was strong and above the rated wind speed, therefore, the B2 wind turbine was operating at the rated capacity for the whole day. Therefore, 1P is a horizontal line, and the same for 2P, 3P, 6P, 9P and 12P. It is also observed that since the FA/SS modes are closely-spaced, it is not possible to distinguish them based on just their frequencies. Therefore, mode shapes are used to separate them. In this study, the FA and SS modes are separated by comparing them to the modal parameters from a reference dataset (i.e., 9:17 on April 22). The MAC values between the identified modes in each dataset with the reference modes are computed and plotted in Figure 14 (a). It is interesting to observe that the black circles are clustered into two groups: top-left and bottom-right clouds. To distinguish the FA/SS modes, a diagonal line (dashed line in Figure 14 (a)) is used to separate them. The FA/SS modes separation results are shown in Figure 14 (b) with colored circles. The FA/SS modes are well separated based on the MAC values in this case.

The evolution of natural frequencies, MAC values, and damping ratios of the identified FA/SS modes on April 22 are shown in Figure 15 (a - c). It is seen that the frequencies of SS mode stay almost constant over time, but the frequencies of FA mode have larger variation. The damping ratios of SS mode are low (< 2%) and also stay roughly constant over time, however, the damping ratios of FA mode are much higher (between 4% and 10%) and vary significantly over the day. The higher identified damping of FA mode also includes the aerodynamic damping since it is in the wind direction, while SS mode is perpendicular to wind and therefore, its damping is not affected by the wind and only represents the structural damping.

To investigate the effects of the yaw angle on the identified modal parameters, the evolution of yaw angle, and the angles of FA/SS modes are shown in Figure 17. The angles of FA/SS modes are defined as the angle between the bending direction of tower and the X axis, as shown in Figure 16 (a). It is seen that the angel of FA/SS modes generally follow the same changing trend as the yaw angle, which means they are highly correlated and their mode shapes depend on the yaw angle, i.e., almost aligned with (for FA mode) and perpendicular to (for SS mode) the wind direction. To further illustrate these relationships, the difference between the angles of SS and FA modes, SS mode and yaw, as well as yaw and FA mode are shown in Figure 18 as a function of time. It is seen that the difference between yaw and angle of FA mode is almost zero over time, which means they are generally collinear. The difference between angle of SS mode and yaw angle is almost 270° over the day, which means they are perpendicular. The same observation can be made between FA and SS modes which are generally perpendicular. The correlation between yaw angle and the angles of FA/SS modes are shown in Figure 19. It is seen that the angles of FA/SS modes are highly correlated with yaw angle and have correlation coefficients of 0.81 and 0.83, respectively.

Two animation videos have been made to illustrate the changing of FA/SS modes with yaw angle over the day of April 22. Sample frames of these videos are shown in Figure 20 and Figure 21, in which the magenta arrows denote the yaw angle. These videos are included in the supplementary files.

For the 2nd FA/SS modes, they cannot be identified with reasonable accuracy in this case, which is probably due to the interference of the 2nd flapwise and edgewise modes of the blades, as well as the 12P, which have frequencies close to the 2nd FA/SS modes.

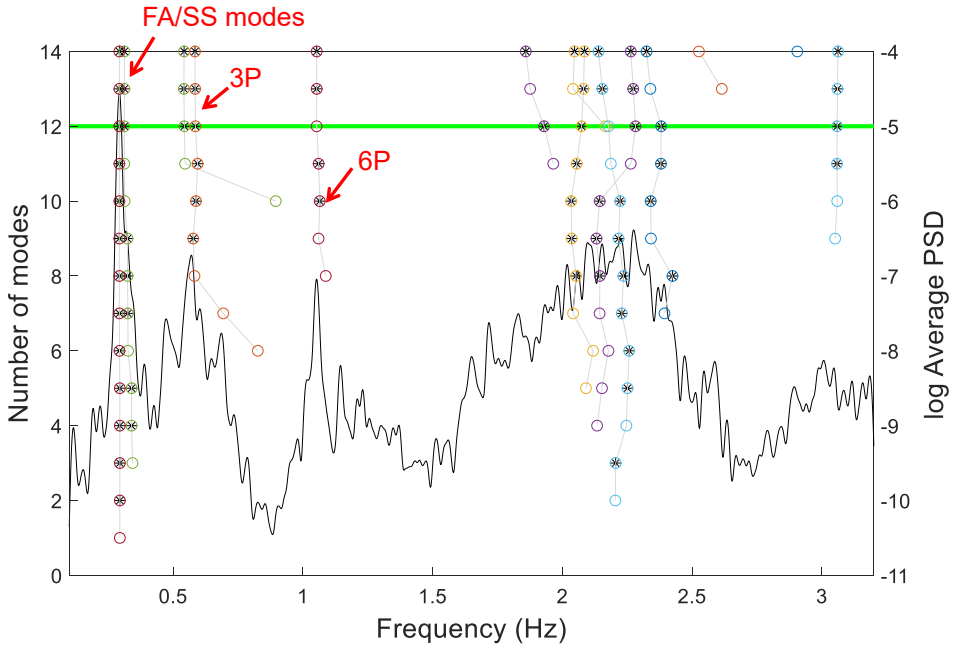

Figure 9. Sample of frequency stabilization diagram at 9:17 on April 22.

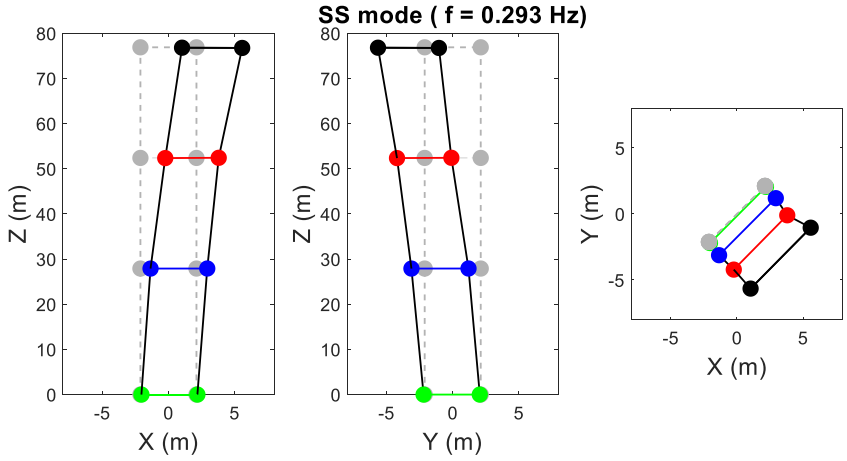

Figure 10. Identified SS mode at 9:17, April 22.

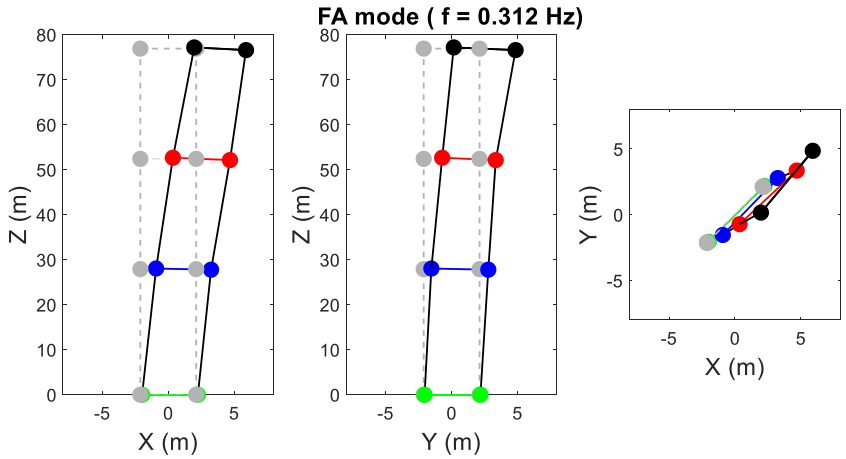

Figure 11. Identified SS mode at 9:17, April 22.

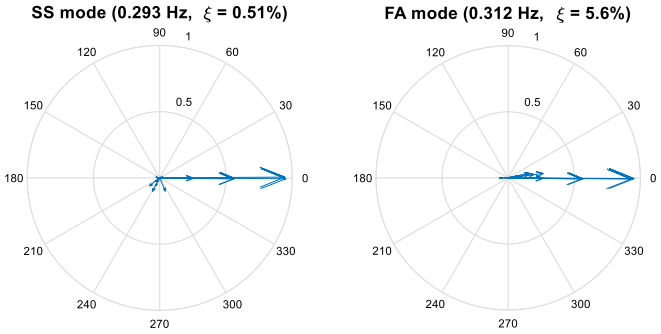

Figure 12. Compass plot of identified SS/FA modes at 9:17, April 22.

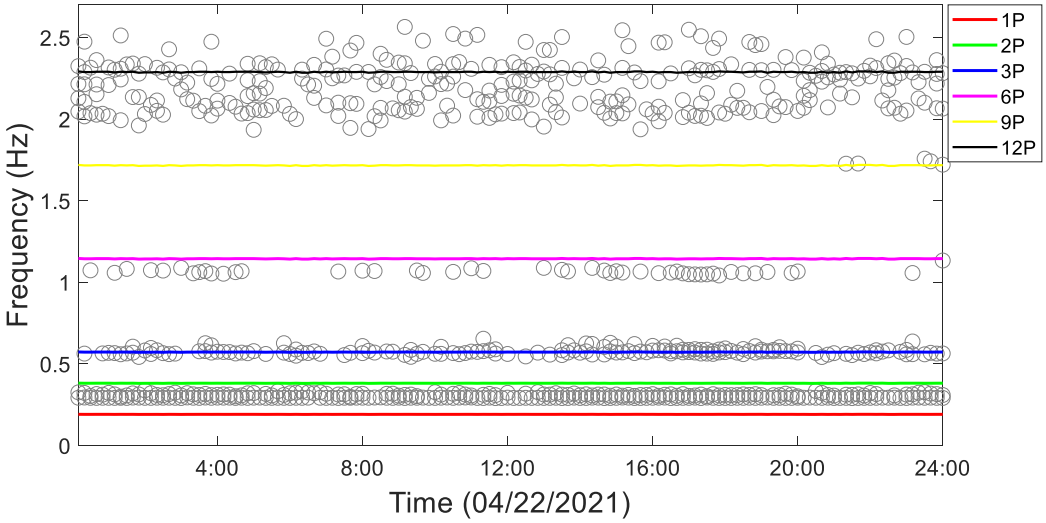

Figure 13. Automated system identification results on April 22.

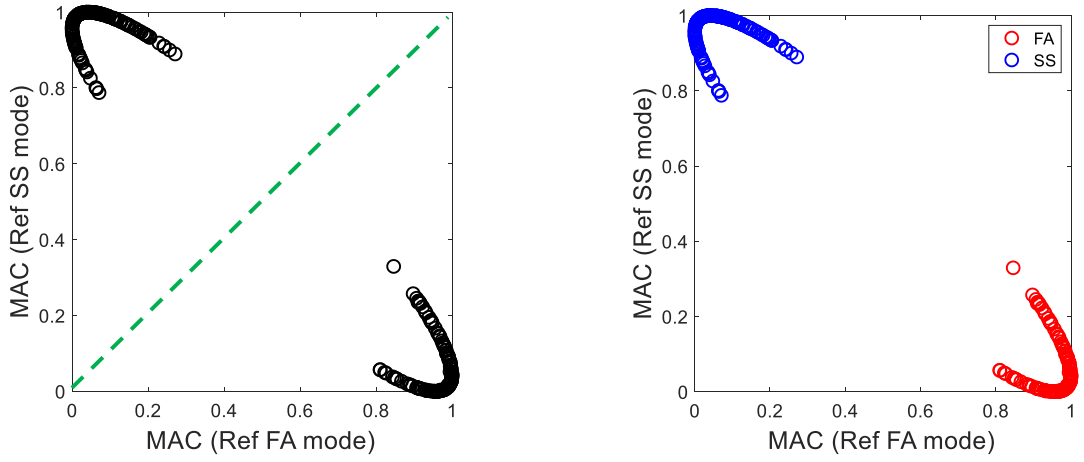

Figure 14. (a) MAC values of each dataset on April 22 with reference FA mode versus that with reference SS mode; (b) FA/SS modes are well separated based on MAC values.

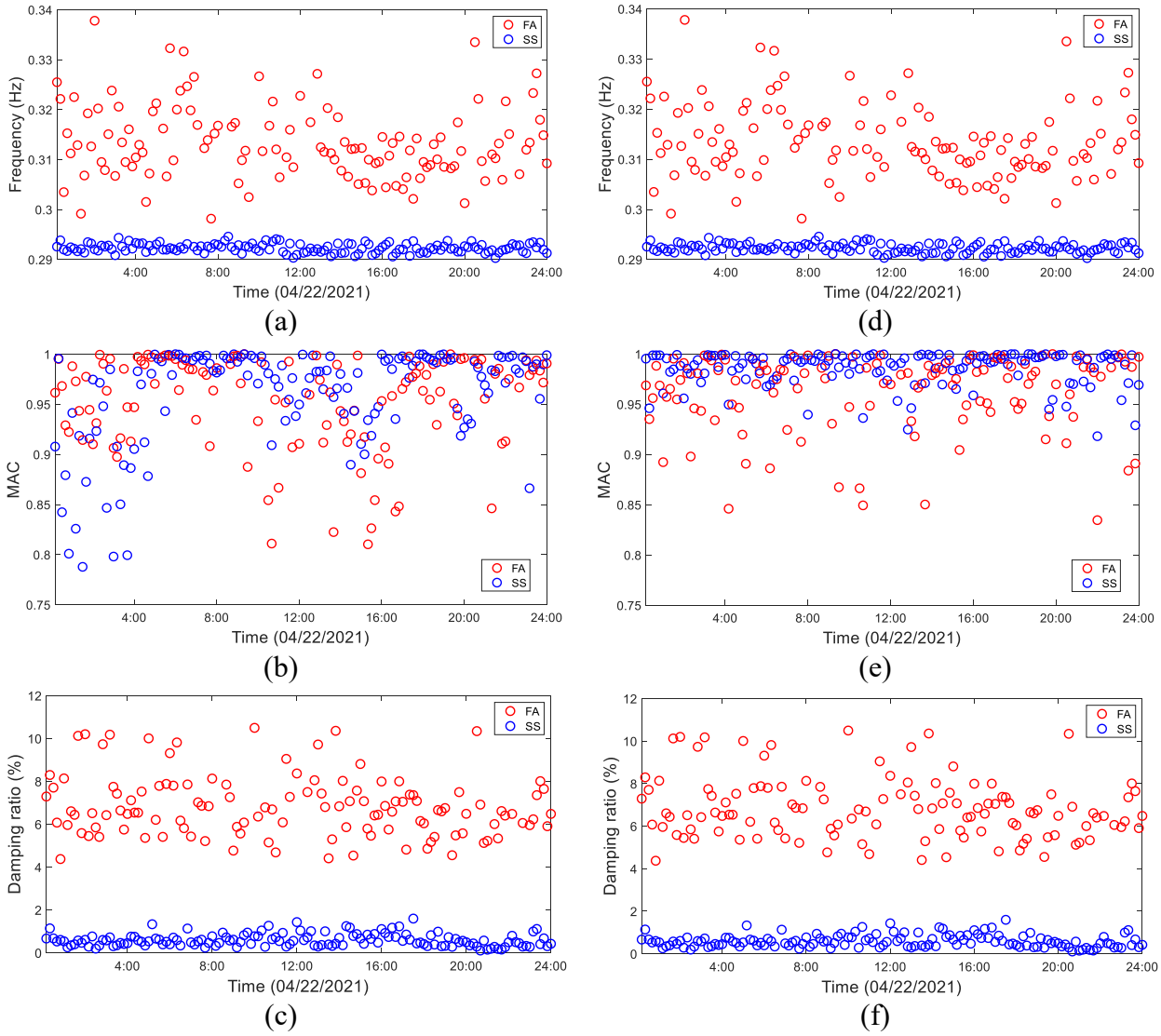

Figure 15. Natural frequencies, MAC and damping ratios evolution of identified FA/SS modes on April 22: (a – c) in global coordinate; (d – f) in FA-SS coordinate.

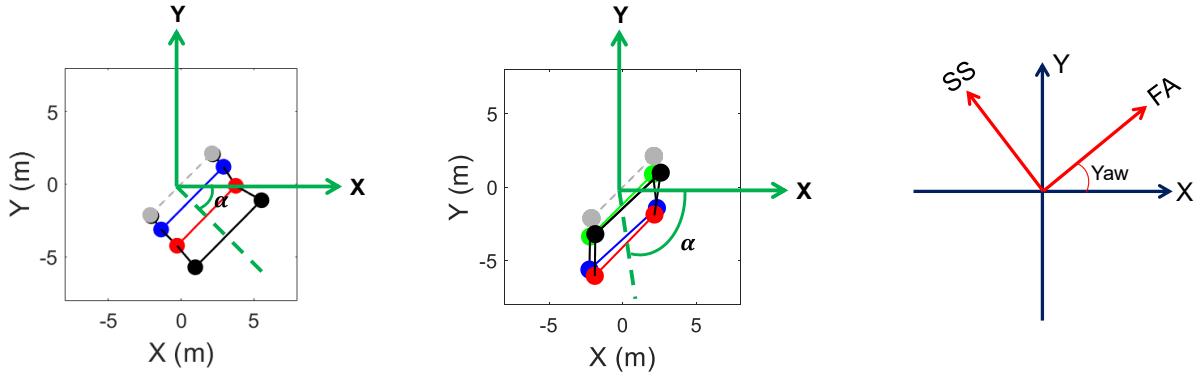

(a) (b) (c)

Figure 16. Definition of angle of 1st FA/SS modes (a) and 2nd FA/SS modes (b); (c) Relationship between global coordinate and FA-SS coordinate.

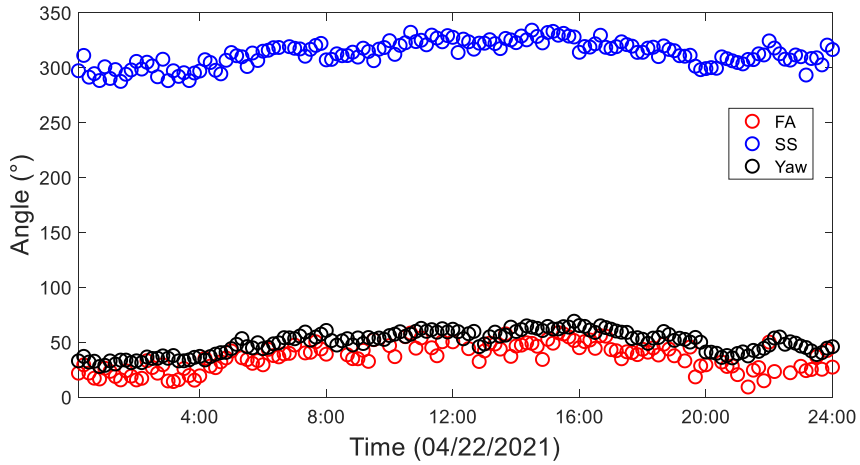

Figure 17. Evolution of Yaw angle, and angles of FA/SS modes.

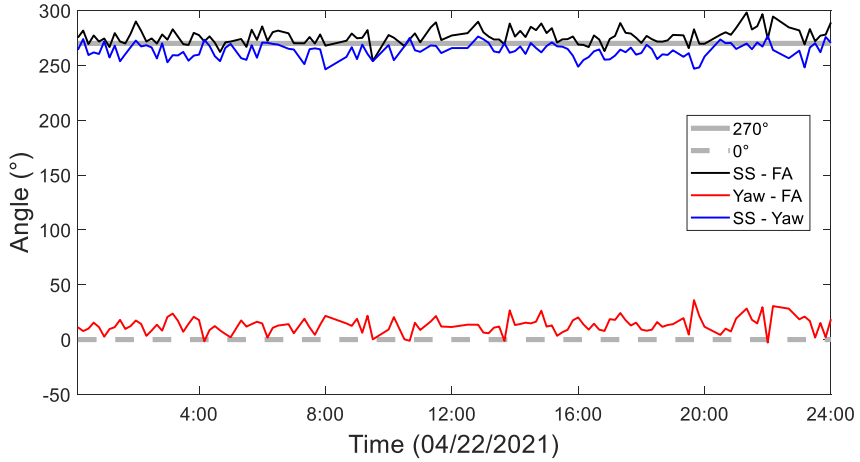

Figure 18. Angle difference evolution between SS and FA modes, SS mode and Yaw, as well as Yaw and FA mode.

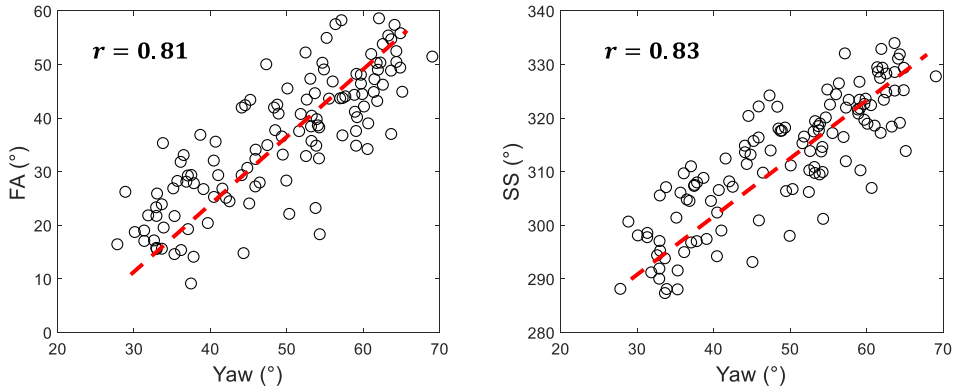

Figure 19. Correlation between yaw angle and FA/SS modes.

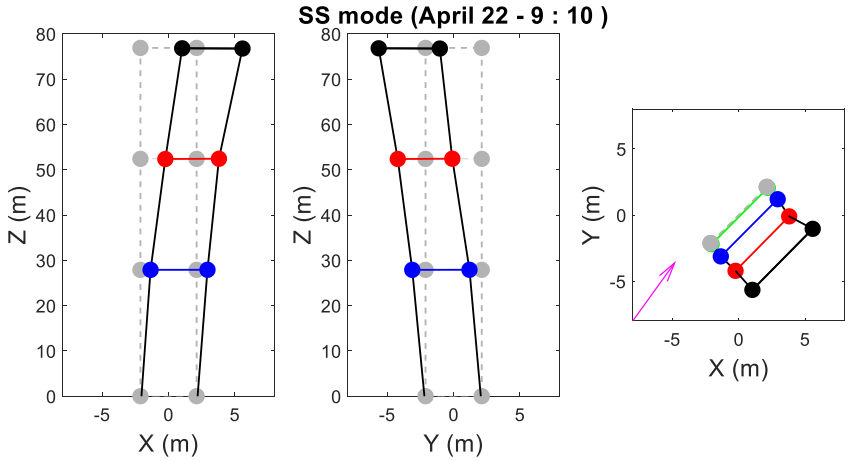

Figure 20. Sample frame of animation video about yaw angle and SS mode.

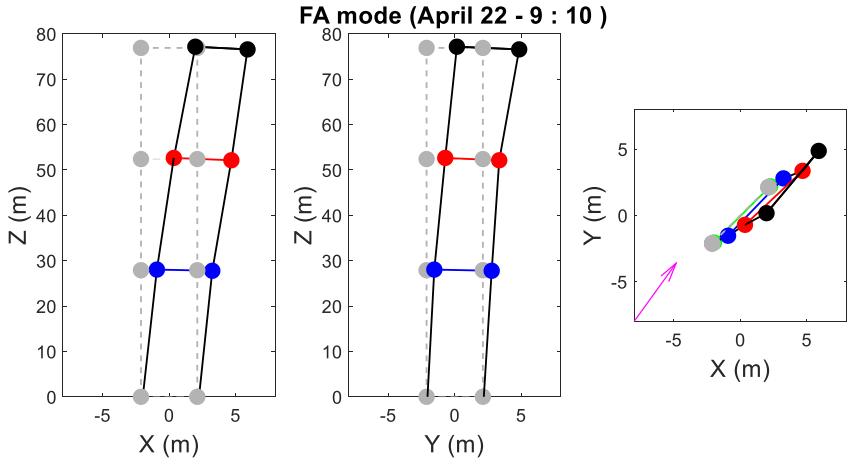

Figure 21. Sample frame of animation video about yaw angle and FA mode.

5.2.2 Modal parameters in FA-SS coordinate

From the previous observations, it is concluded that the mode shapes of FA/SS modes are closely correlated to the yaw angle, and their bending directions change over time. Therefore, the MAC values between different datasets are affected by the yaw angle. To alleviate this effect, the identified modes are transformed from the fixed global coordinate to the time-varying FA-SS coordinate as shown in Figure 16 (c), where the FA mode will have the same bending direction as FA axis, and SS mode is collinear with SS axis. The similar plot of MAC values between all the identified modes with the reference modes (at 9:17) based on FA-SS coordinate are shown in Figure 22. It is seen that two clouds of circles are further clustered within each group, and two modes can be easily separated using the diagonal line. The corresponding evolution of natural frequencies, MAC values, and damping ratios are shown in Figure 15 (d – f). Comparing to Figure 15 (a – c), it is evident that the MAC values are larger and closer to 1 after the transformation to the FA-SS coordinate, with most of the MAC values higher than 0.95. This means that the identified modes are highly consistent over different datasets, even though the mode shapes are affected significantly by the wind direction and yaw angle.

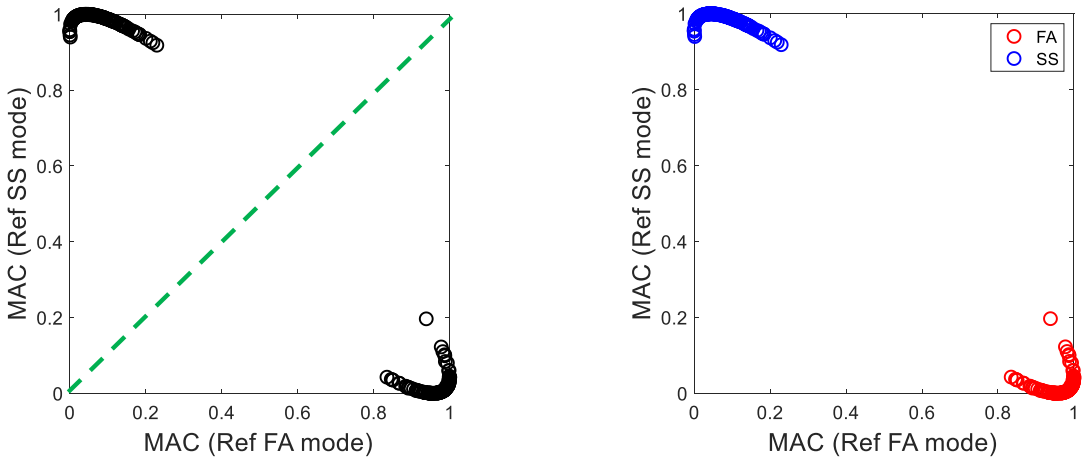

(a) (b)

Figure 22. (a) MAC values with reference FA mode versus that with reference SS mode based on FA-SS coordinate; (b) FA/SS modes are well separated based on MAC values.

5.2.3 Modal expansion based on FA and SS modes

To study the modal contribution of the identified FA/SS modes, as well as to investigate whether they can be used to construct the response of sensors, a modal expansion approach is used. In the modal expansion approach, the modal contribution is first estimated and then used to predict the response at measured locations. The same dataset measured at 9:17 am on April 22 is used here. First, the acceleration data are filtered through a bandpass filter between 0.24 Hz and 0.36 Hz to focus on the contribution of the FA/SS modes. The FAS of filtered acceleration data measured at accelerometers A1 - A6 are shown in Figure 23. Then the modal coordinates $\hat{\mathbf{q}}(t)$ are computed based on the filtered acceleration $\mathbf{u}(t)$ and the identified mode shape matrix of FA and SS modes $\boldsymbol{\Phi}_u$:

$$\hat{\mathbf{q}}(t) = \boldsymbol{\Phi}_u^{+}\mathbf{u}(t) \tag{19}$$

where $\boldsymbol{\Phi}_u^{+}$ denotes the pseudo-inverse of mode shape matrix $\boldsymbol{\Phi}_u$. The evaluated modal coordinate $\hat{\mathbf{q}}(t)$ of FA/SS modes are shown in Figure 24. It is seen that the amplitude of SS mode is generally larger than that of FA mode, and both amplitudes change drastically over time.

After the modal coordinate $\hat{\mathbf{q}}(t)$ is computed, then it is used to predict the total response by combining the contribution of FA and SS modes:

$$\hat{\mathbf{u}}(t) = \boldsymbol{\Phi}_u\hat{\mathbf{q}}(t) \tag{20}$$

where $\hat{\mathbf{u}}(t)$ refers to the predicted response. The predicted and measured acceleration responses are compared in Figure 25 for channels A1-X and A1-Y. It is seen that the predictions match the measurements very well. Another interesting observation is that the phase plot of acceleration channels in Figure 25 resembles ellipses with varying axis lengths and directions in time. These are due to the changing amplitude and contribution of FA and SS modes over time. An animation video is made about the modal expansion results which are included in the supplementary files. A sample frame of the animation video is shown in Figure 26. It is interesting to observe that the contribution of SS mode can be regarded as the abscissa, and that of the FA mode is close to the ordinate, therefore, their total contribution presents different ellipses with different sizes and directions based on their individual amplitudes. The relative root-means-square error (RRMSE) is defined to measure the accuracy of the response prediction using modal expansion:

$$\text{RRMSE}(\hat{\mathbf{u}}) = \frac{\text{RMS}(\hat{\mathbf{u}} - \mathbf{u})}{\text{RMS}(\mathbf{u})} \times 100\% \tag{21}$$

where $\hat{\mathbf{u}}$ and $\mathbf{u}$ denote the predicted and true response time histories, respectively. The RRMSE for channels at A1 – A6 are summarized in Table 1. It is seen that the RRMSE are very small, which means that the identified modes can be treated as time invariant, and the measured data can be accurately decomposed into the contribution of the FA and SS modes.

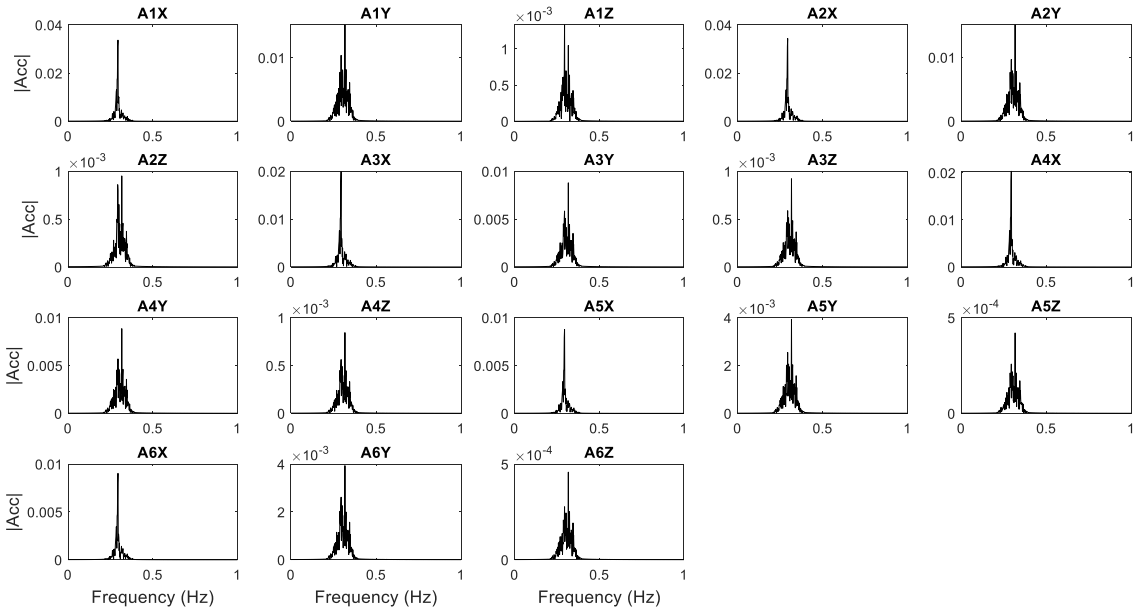

Figure 23. FAS of acceleration filtered between 0.24 and 0.36 Hz.

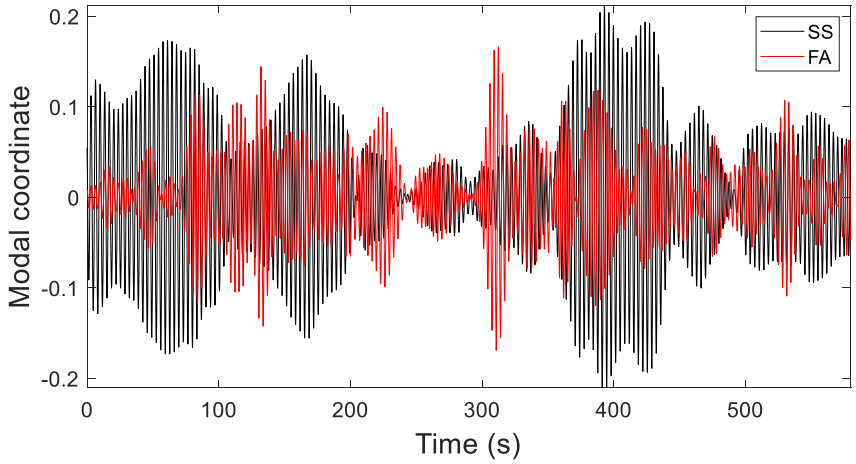

Figure 24. Modal coordinate of FA/SS modes.

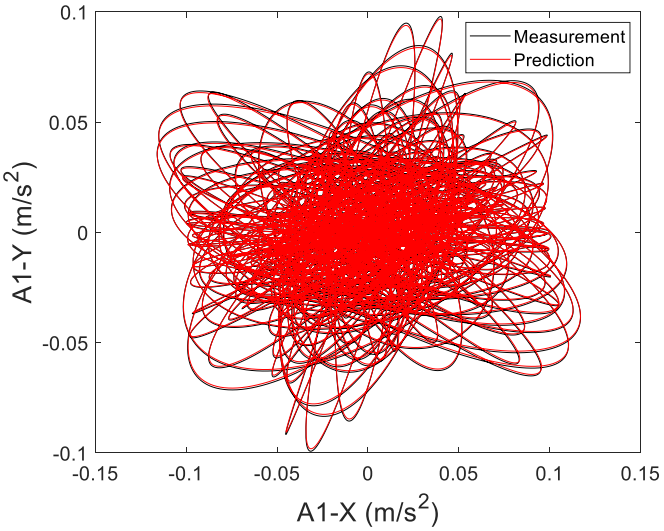

Figure 25. Comparison of acceleration predictions using modal expansion with measurements.

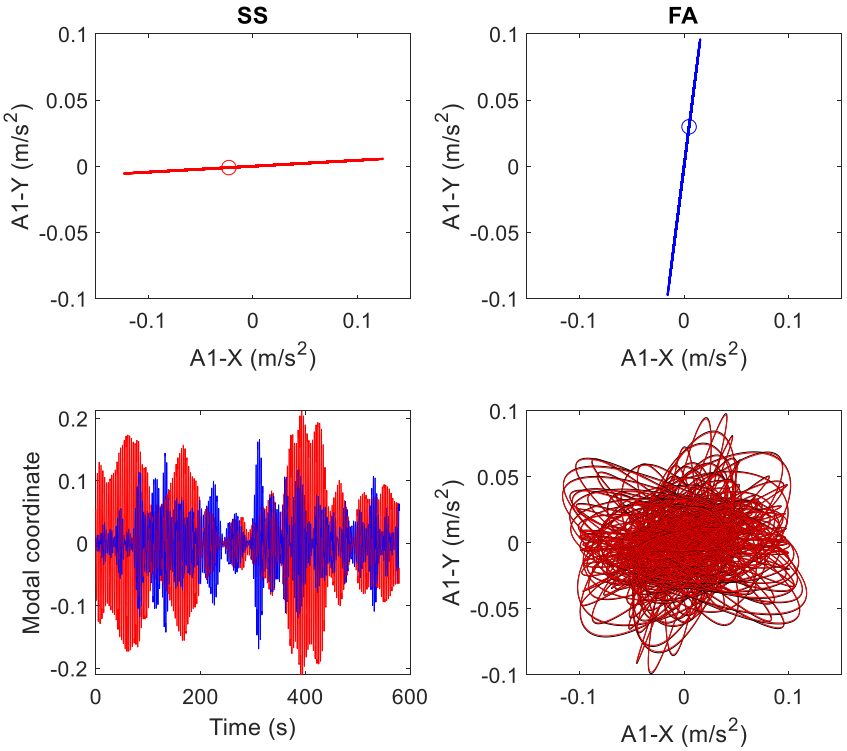

Figure 26. Sample frame of animation video about modal expansion results.

Table 1. RRMSE (%) of acceleration predictions using modal expansion.

	X	Y
A1	0.35	1.26
A2	0.54	1.23
A3	0.90	2.05
A4	0.56	2.19

A5	1.98	6.69
A6	1.63	6.72

5.3 System identification over a day with varying rotor speed (April 25)

5.3.1 System identification results

The automated system identification in this section follows the same procedure as for April 22. The purpose of investigating the data on April 25 is that the wind direction and wind speed change rapidly in this day, which provided a rapidly varying environment on the wind turbine. This potentially causes challenges on the automated system identification. A sample frequency stabilization diagram at 13:17 on April 25 is shown in Figure 27, and the identified SS and FA modes are illustrated in Figure 28 and Figure 29, respectively. A similar strategy based on MAC values is used to separate the FA/SS modes, which is shown in Figure 30 (a) by choosing the modes identified at 13:17 as the reference modes, and the separation results are shown in Figure 30 (b). It is seen that the black circles are lined up as a diagonal line and there is not an evident gap to separate them into two groups. This means that there is so much variation on the FA/SS modes due to the drastically changing yaw angle, these modes cannot be perfectly separated based on the MAC values, i.e., the FA modes in some datasets are close to the SS modes in other datasets. Another reason is that some 3P or 2P spurious modes are also misclassified as the FA/SS modes because the rotor speed changes rapidly and 3P or 2P have crossings with the natural frequencies of FA/SS modes.

The evolution of identified frequencies, MAC values, and damping ratios of the FA/SS modes on April 25 are shown in Figure 31 (a – c). Similar to the results observed on April 22, natural frequencies of SS mode general stay stable, while those of FA mode vary significantly over time. The damping ratios of SS mode are generally stable and lower than those of FA mode. The damping ratios of FA mode are high and change rapidly due to the aerodynamic damping. However, since the FA/SS modes are not perfectly separated, some frequencies and damping ratios of these modes are mixed together, and the MAC values are relatively low. The automated system identification results on April 25 are shown in Figure 32, superposed with 1P, 2P, 3P, 6P, 9P, and 12P frequencies obtained from SCADA. It is seen that, due to the rapidly-varying rotor speed, 1P - 12P are changing drastically as well. 2P and 3P have several crossings with FA/SS modes, which would potentially magnify the response amplitude due to modal resonance. The frequencies of the FA/SS modes stay constant over time, and the 3P, 6P, 9P, and 12P are also estimated and follow the same trend as the SCADA information.

The evolution of the dominant directions (angles) of the FA/SS modes together with the turbine yaw angle are shown in Figure 33. It is seen that the yaw angle changes drastically over this day due to the rapidly varying wind conditions, and angles of the FA/SS modes generally follow the trend of yaw angle. The FA/SS modes stay generally perpendicular to each other over this day. Two animation videos are made to visualize the evolution of yaw angle and the mode shapes of FA/SS modes, which are included in the supplementary materials. Two sample frames of these videos are shown in Figure 34 and Figure 35.

Similar to April 22, the 2nd FA/SS modes cannot be identified with reasonable accuracy on April 25, due to the interference of the 2nd flapwise and edgewise modes of the blades, as well as the 12P, which has frequency close to the 2nd FA/SS modes.

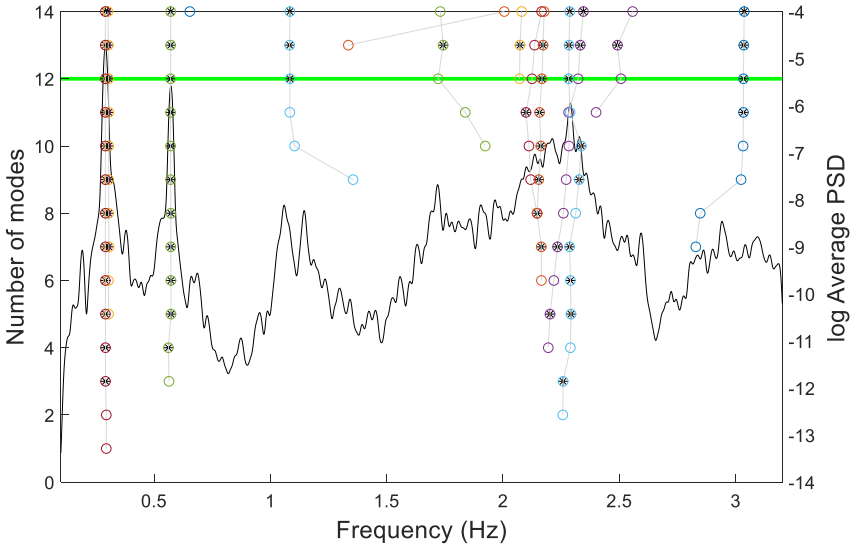

Figure 27. Sample of frequency stabilization diagram at 13:17 on April 25.

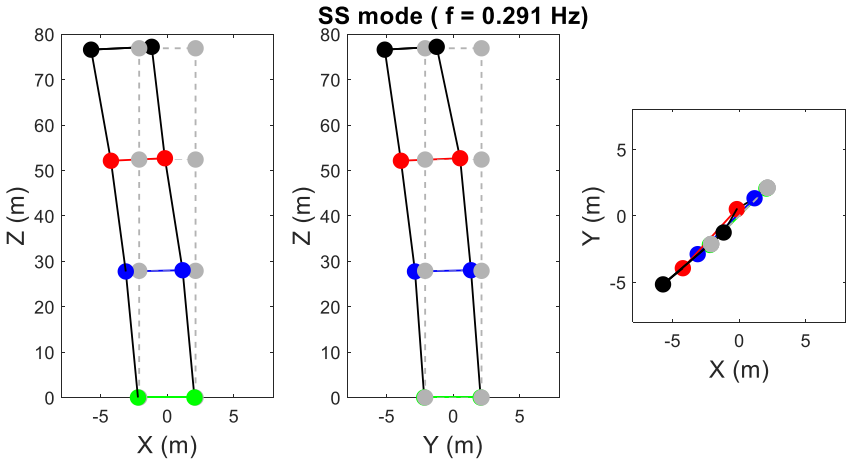

Figure 28. Identified SS mode at 13:17, April 25.

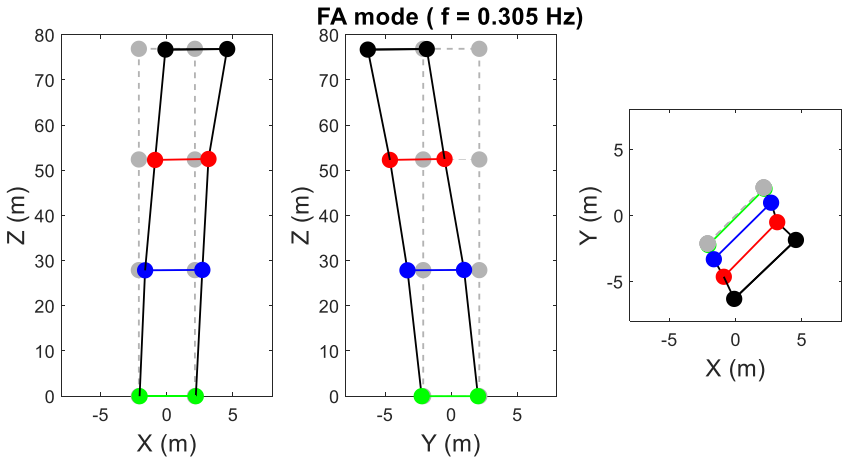

Figure 29. Identified FA mode at 13:17, April 25.

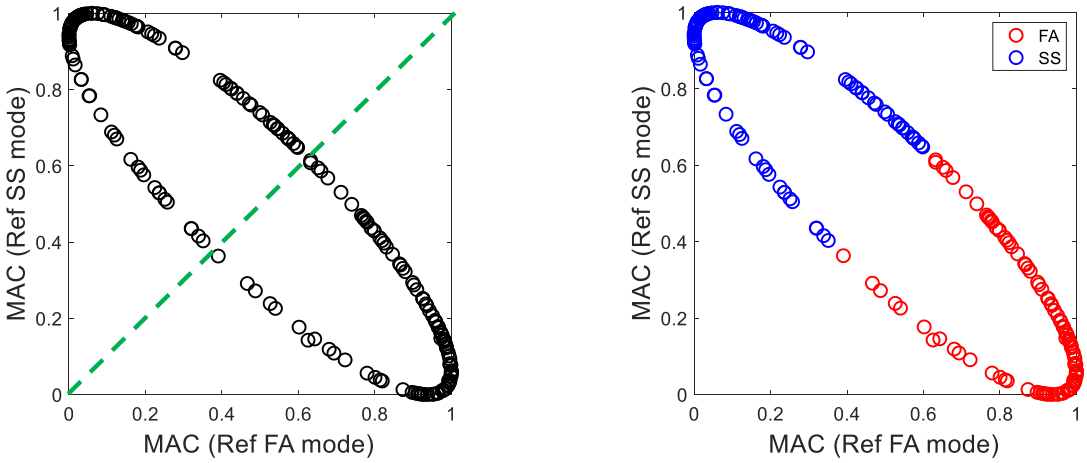

(a) (b)

Figure 30. (a) MAC values of each dataset on April 25 with reference FA mode versus that with reference SS mode; (b) FA/SS modes separation results.

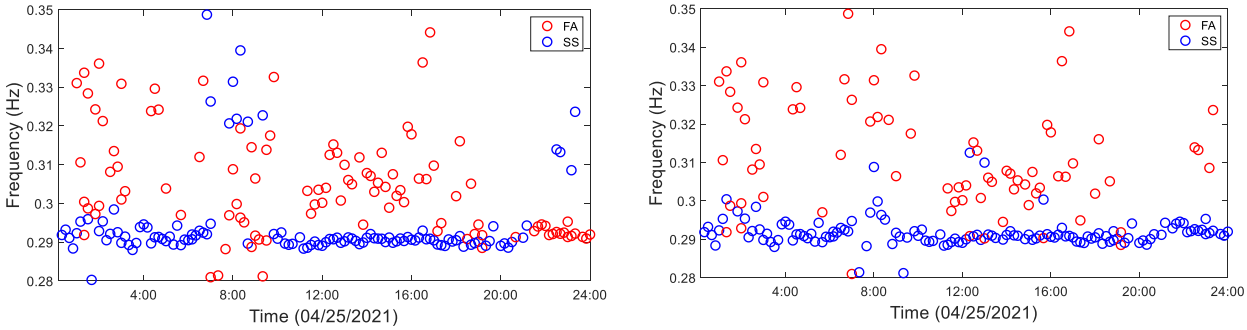

(a) (d)

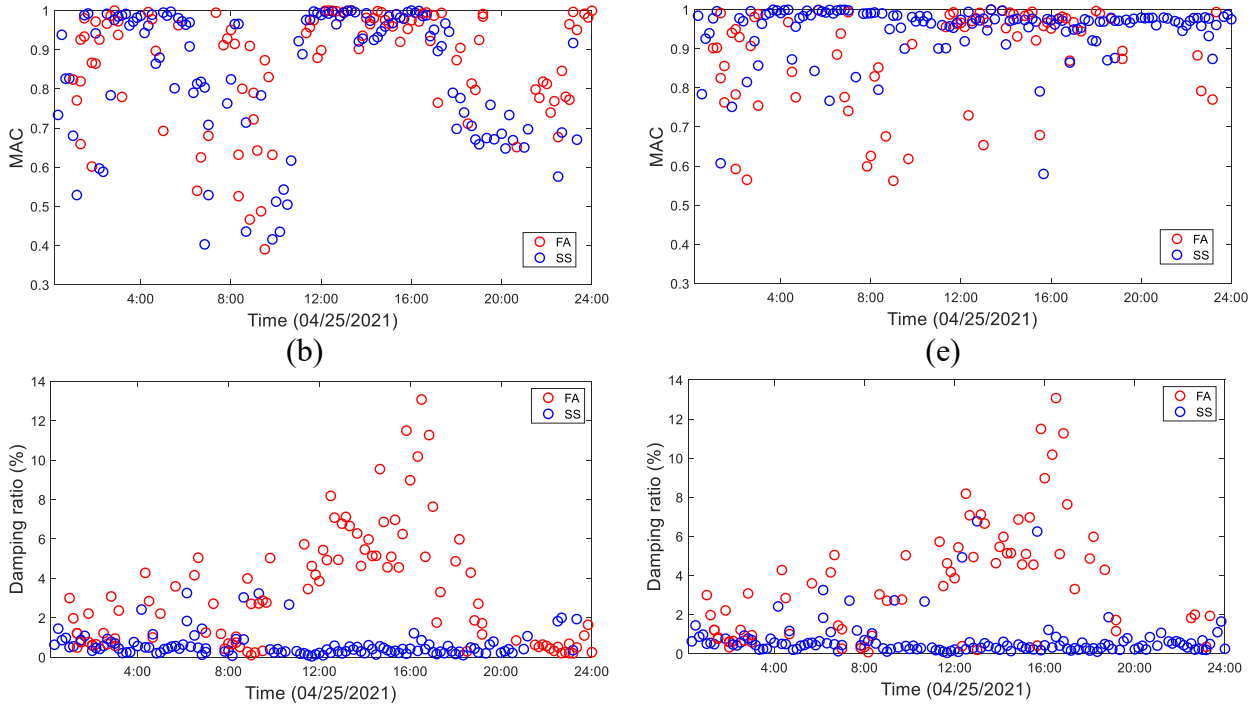

Figure 31. Frequencies, MAC and damping ratios evolution of identified FA/SS modes on April 25: (a – c) in global coordinate; (d – f) in FA-SS coordinate.

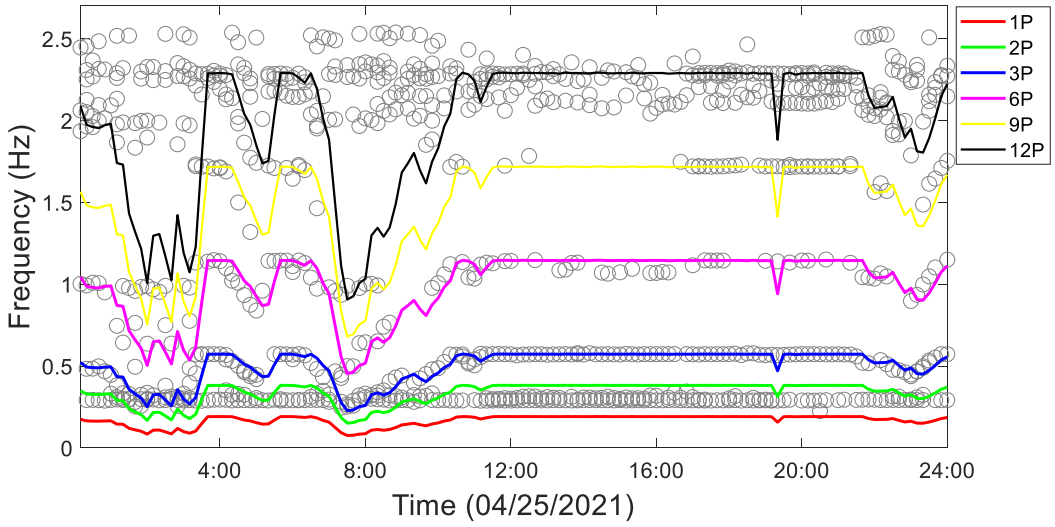

Figure 32. Automated system identification results on April 25.

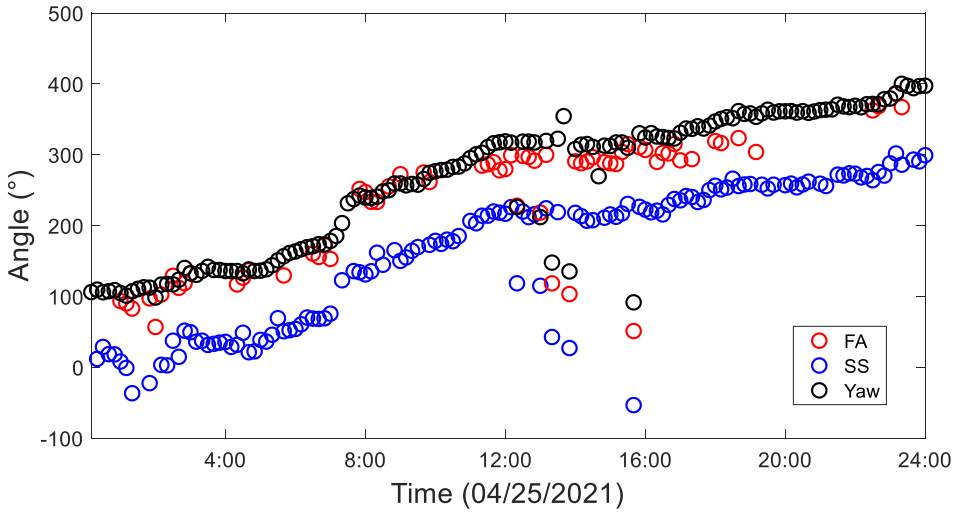

Figure 33. Evolution of Yaw angle, and angles of FA/SS modes.

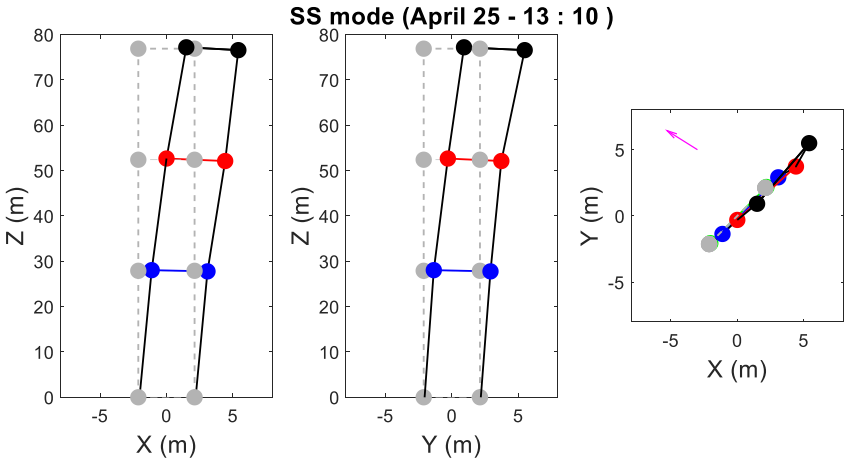

Figure 34. Sample frame of animation video of yaw angle and SS mode.

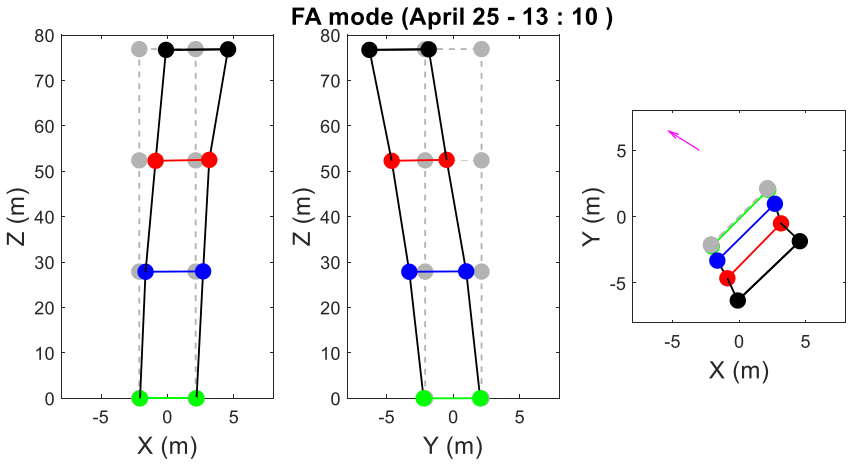

Figure 35. Sample frame of animation video of yaw angle and FA mode.

5.3.2 Modal parameters in FA-SS coordinate

The identified FA/SS modes cannot be well separated based on the MAC values in global coordinate due to the effects of varying yaw angle (Figure 30). In this section, the identified FA/SS modes are transformed to the FA-SS coordinate to improve the separation accuracy, similar to the approach in section 5.2.2. The separation results based on the MAC values in FA-SS coordinate are shown in Figure 36. It is seen that the black circles are more clustered into the top-left and bottom-right corners, and less circles are scattered in the middle area. To further improve the classification accuracy, the data in the middle area are discarded, and the circles below the line $y = x - 0.3$ are classified as FA mode, and the circles above the line $y = x + 0.3$ are classified as SS mode. This improves the separation accuracy and reduces misclassification. The frequencies, MAC and damping ratios evolution based on the new classification results are shown in Figure 31 (d – f). Compared to Figure 31 (a – c), it is evident that the classification accuracy has been improved evidently, for example, some of the SS modes between 21:00 to 24:00 were misclassified as FA modes, but now they are accurately classified as the SS mode. Most of the FA/SS modes are classified correctly, and the MAC values are larger and closer to one. Similar to the observation in section 5.2.2 for April 22, the FA mode has larger variability in frequency, and its damping ratios are larger than those of SS mode due to the aerodynamic damping.

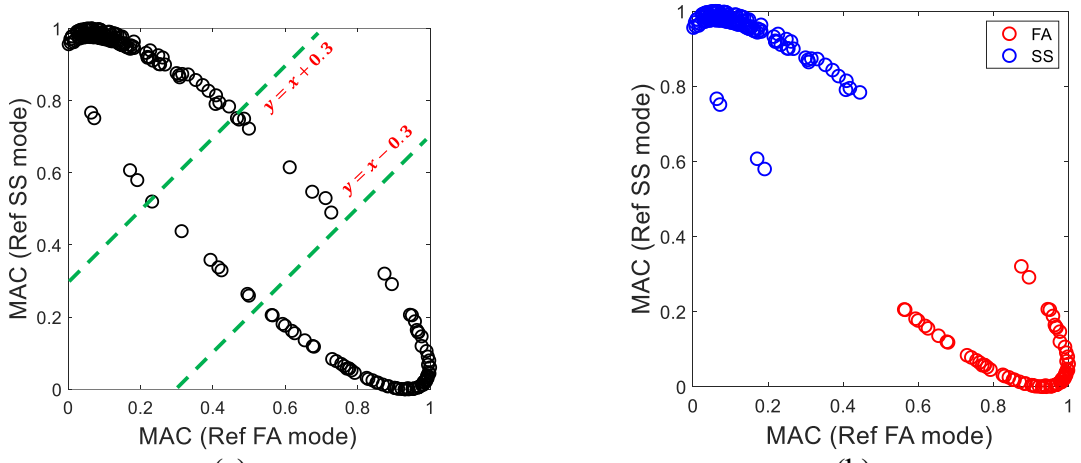

Figure 36. (a) MAC values with reference FA mode versus that with reference SS mode based on FA-SS coordinate; (b) FA/SS modes separation is improved.

5.3.3 Response amplification due to modal resonance

In this section we investigate whether the overlap of 3P frequency with FA/SS modes has caused any response amplification. From the system identification results in Figure 32, it is seen that there are two regions where 3P overlaps the natural frequencies of the FA/SS modes, which is shown in the shaded area in Figure 37. Modal resonances are potentially present in these regions which will magnify the response amplitude. To verify the evolution of response amplitude over time, the room-mean-square (RMS) of acceleration data is plotted against the wind speed in Figure 38 for accelerometers A1 – A3 and in Figure 39 for A4 – A6. It is worth noting that the acceleration data are filtered through a bandpass filter between 0.24 to 0.36 Hz to

focus on the response of the FA/SS modes. It is seen that the acceleration RMS are amplified in the shaded time region, which belongs to one of the two potential resonance regions. To further investigate the changing of response amplitude against the wind speed, the |log (RMS)| divided by wind speed is shown in Figure 40 for A1 – A3 and in Figure 41 for A4 – A6. Two noticeable peaks are present which are located exactly at the two modal resonance regions, which means the acceleration response are magnified due to the modal resonance and the effect of 3P.

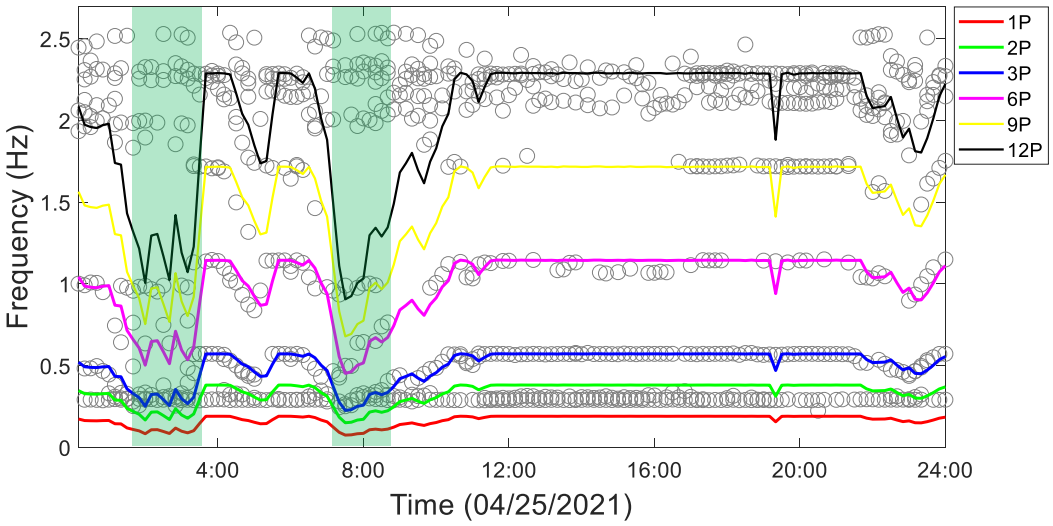

Figure 37. Potential modal resonance of FA/SS modes due to 3P on April 25.

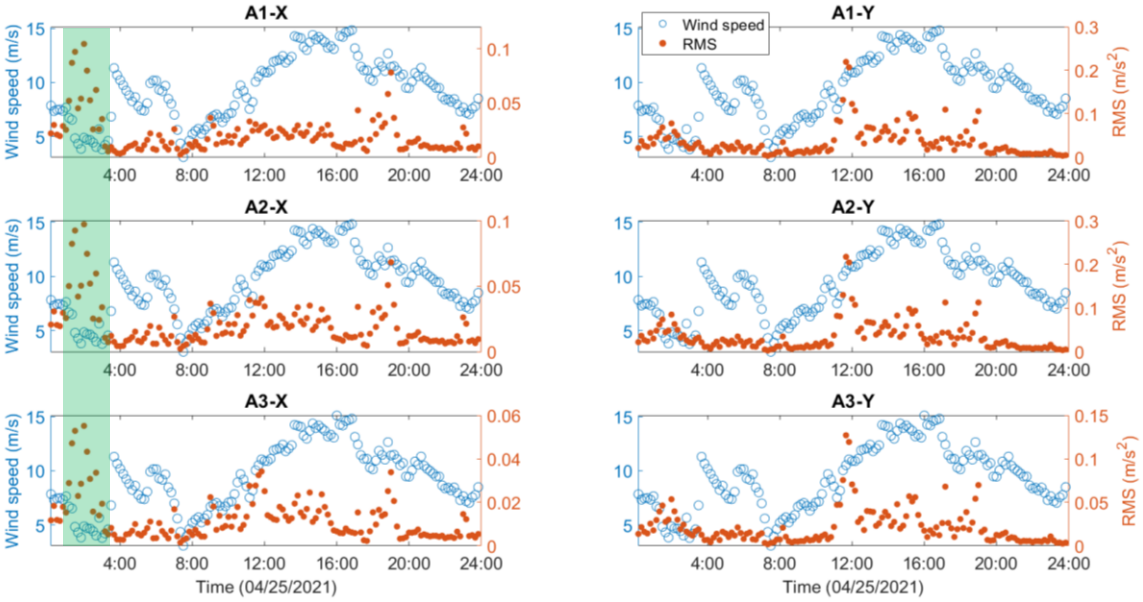

Figure 38. Evolution of acceleration RMS versus wind speed (A1 – A3).

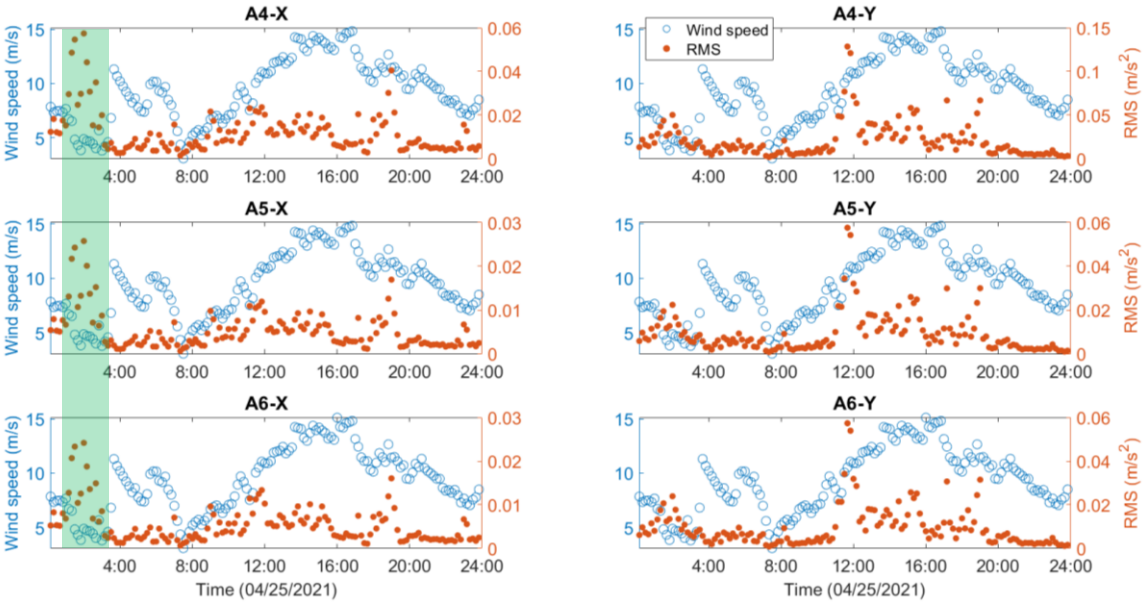

Figure 39. Evolution of acceleration RMS versus wind speed (A4 – A6).

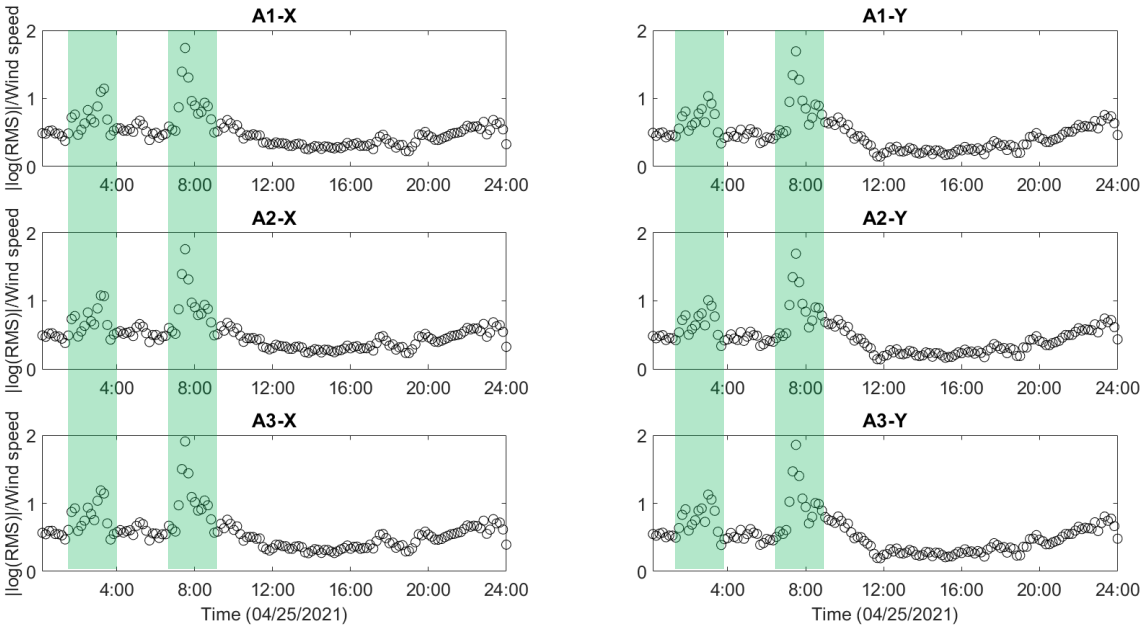

Figure 40. Evolution of |log (RMS)|/wind speed (A1 – A3).

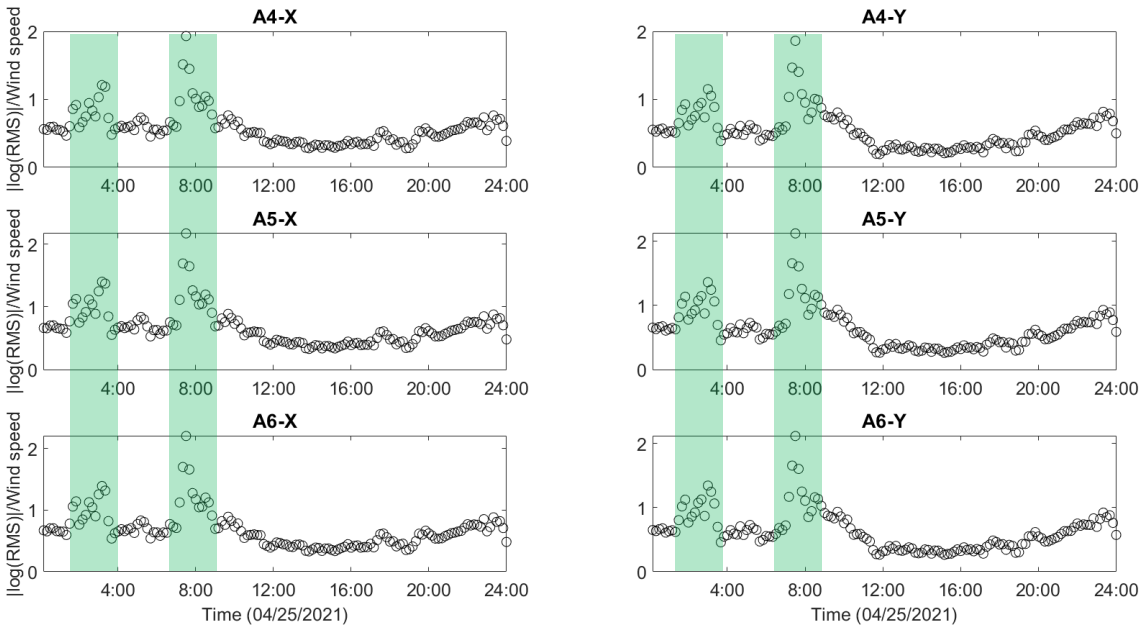

Figure 41. Evolution of |log (RMS)|/wind speed (A4 – A6).

5.4 System identification over a day with parked turbine (July 6)

5.4.1 Identification of 1st FA/SS modes

The same automated system identification process is implemented here to identify the modal parameters of B2 offshore wind turbine on July 6. The significance of data on July 6 is that the turbine is parked during the tropical storm Elsa, which provides a good opportunity to identified modal parameters without the effect of rotating rotor. The frequency stabilization diagram at 8:31 on July 6 is shown in Figure 42, where the 2nd SS and FA modes are present. The automated system identification results are shown in Figure 43. It is seen that, unlike the results on April 22 and 25, in addition to the 1st FA/SS modes, the 2nd SS and FA modes are also reliably identified over this day. The 2nd FA/SS modes cannot be accurately identified when the turbine is in operation due to the interference of 12P and the modes of blades which are close to the 2nd SS and FA modes. The results of the 2nd FA/SS modes are discussed in next section. The identified SS and FA modes are shown in Figure 44 and Figure 45, respectively. A similar strategy based on the MAC values is used to separate the FA/SS modes by choosing the results at 8:31 as the reference modes, as shown in Figure 46. It is seen that the data are not clearly grouped into two clusters, and some circles are scattered in the middle area. To reduce the classification error, the circles in the middle area are discarded, and the circles below the line $y = x - 0.3$ are classified as the FA mode, and the circles above the line $y = x + 0.3$ are classified as the SS mode.

The evolution of the identified natural frequencies, MAC values, and damping ratios on July 6 are shown in Figure 47. Unlike previous observations when the turbine was in operation, the frequencies of 1st FA/SS modes are closer together and show similar variations under parked conditions. The frequency of the FA mode is smaller than previous results (around 0.29 Hz compared to ~0.31 Hz), probably because of the effect of aerodynamics and the fact that the tower stiffness is increased in higher wind speed. Another interesting observation is that, unlike

the results on April 22 and 25, the damping ratios of the FA mode now are comparable to those of the SS mode, which are smaller than the results on April 22 and 25, because the aerodynamic damping is absent, and the damping only represents the structural damping. The angles evolution of the identified FA/SS modes on July 6 is shown in Figure 48. It is seen that dominant direction of FA/SS modes generally stays constant because the turbine is parked, and the yaw angle is constant. The angle difference between SS and FA modes is almost 270°, confirming the orthogonality of these modes. Two animation videos of the mode shape evolution of the FA/SS modes on July 6 are made and included in the supplementary files.

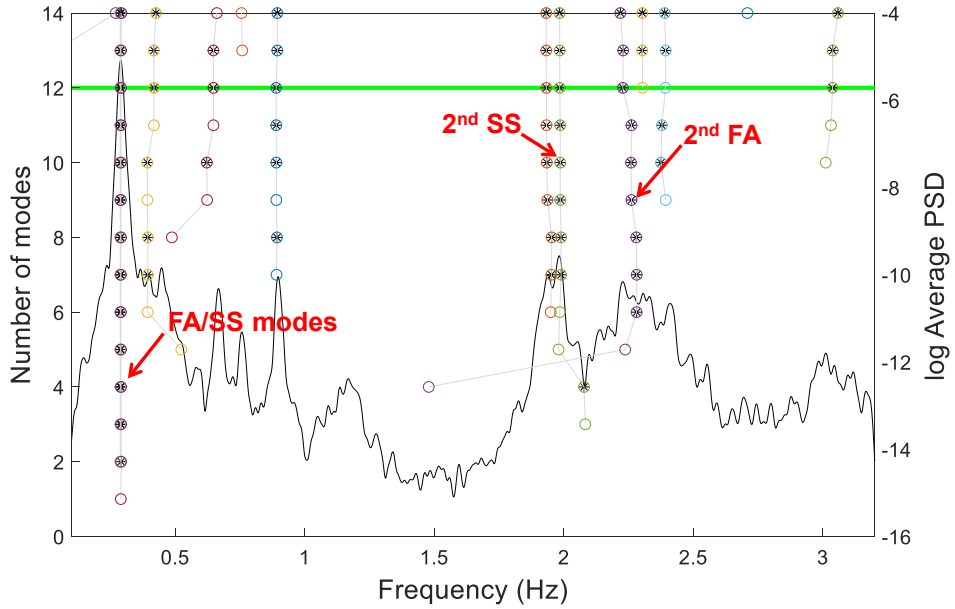

Figure 42. Sample of frequency stabilization diagram at 8:31 on July 6.

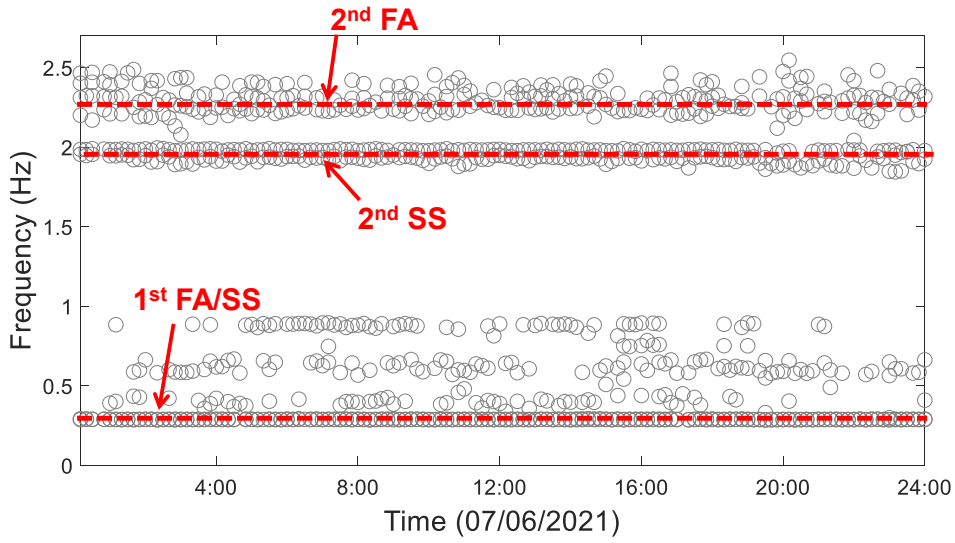

Figure 43. Automated system identification results on July 6.

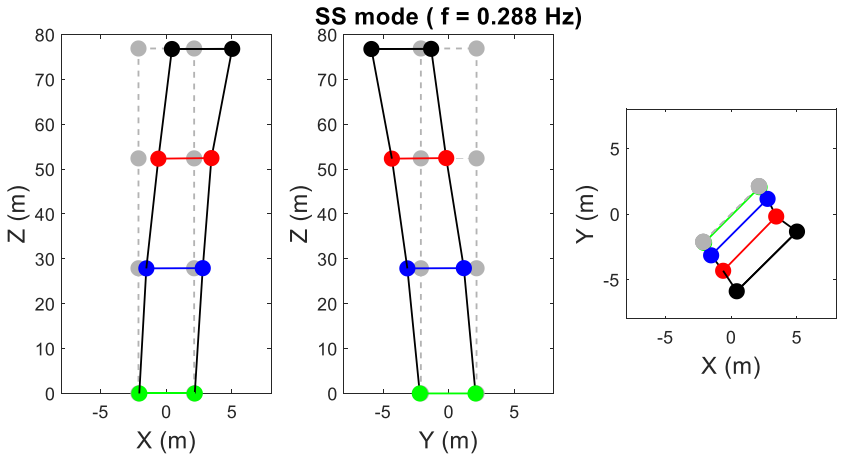

Figure 44. Identified SS mode at 8:31, July 6.

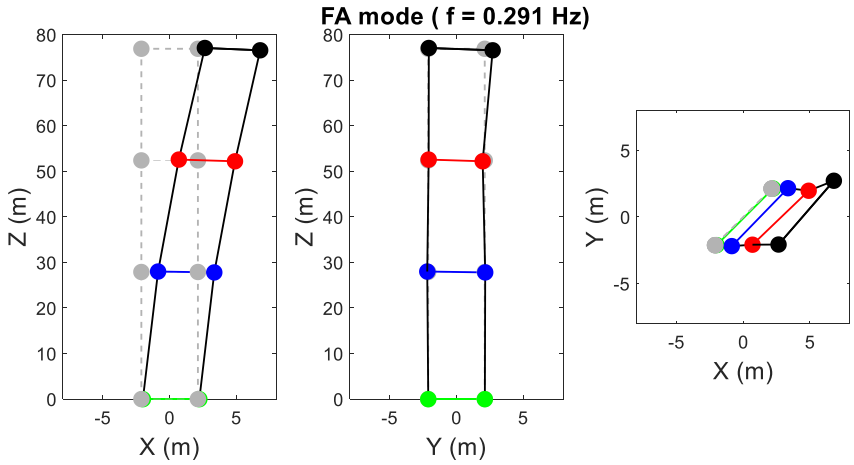

Figure 45. Identified FA mode at 8:31, July 6.

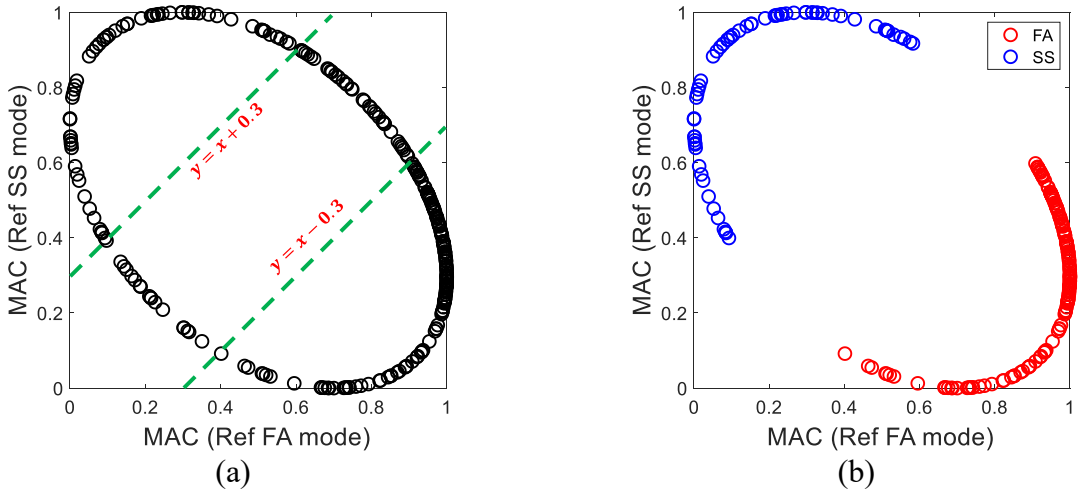

Figure 46. (a) MAC values with reference FA mode versus that with reference SS mode; (b) Separation results.

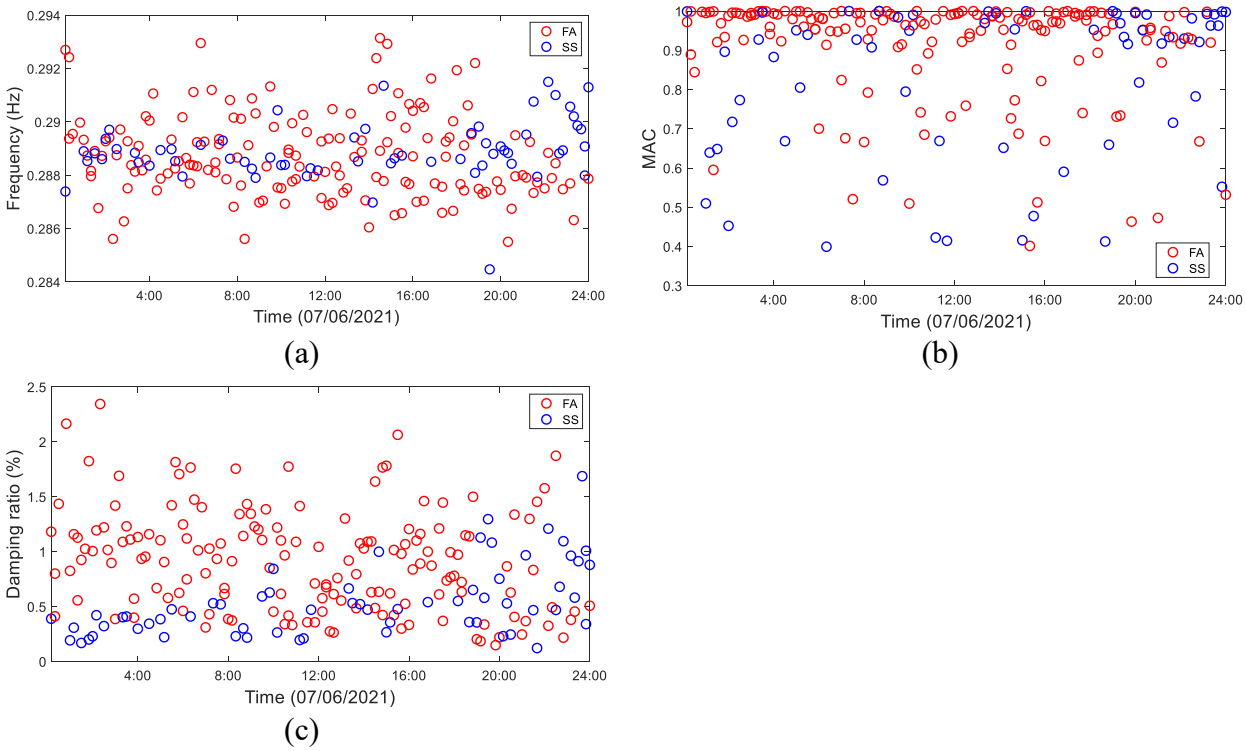

Figure 47. Frequencies, MAC and damping ratios evolution of identified FA/SS modes on July 6.

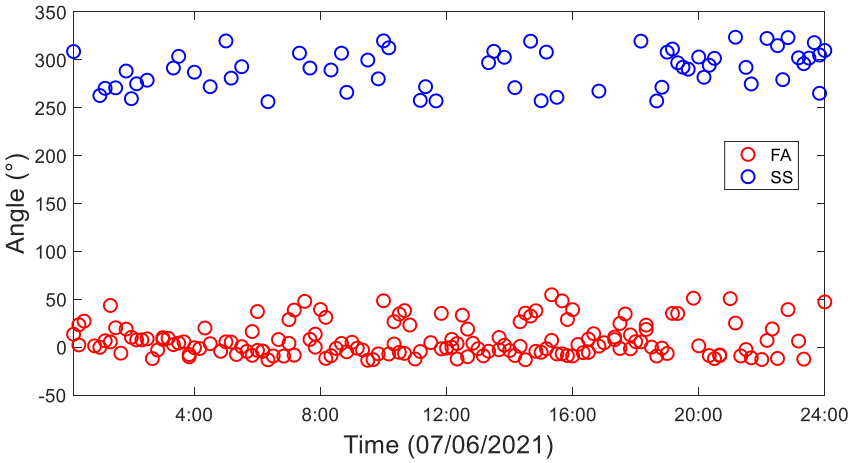

Figure 48. Evolution of angles of FA/SS modes on July 6.

5.4.2 Identification of 2nd FA/SS modes

The identified 2nd SS and FA modes are plotted in Figure 49 and Figure 50, respectively. The complex valued mode shapes are shown as compass plots in Figure 51. It is seen that components of both 2nd SS/FA modes are almost collinear indicating they are classically damped. Because the natural frequencies of 2nd SS/FA modes are different (~ 2.0 Hz for 2nd SS mode and ~ 2.3 Hz for 2nd FA mode), they can be easily separated based on their frequencies. However,

multiple spurious modes whose frequencies are close to the 2nd FA/SS modes are obtained in the identification results, which can be observed in Figure 42 and Figure 43. To remove the spurious modes, the MAC values with the reference modes (at 8:31) are used here and modes with MAC values smaller than 0.6 are discarded. This process is shown in Figure 52. From Figure 52 (b), it is seen that the 2nd SS modes are identified with high consistency with MAC values close to one, while MAC values of 2nd FA modes are smaller and show larger variations. The evolution of the natural frequencies and damping ratios of 2nd FA/SS modes are shown in Figure 53 and Figure 54, respectively. The frequencies of 2nd SS mode stay very stable over time, while those of 2nd FA mode have noticeable variations. The damping ratios of the 2nd FA/SS modes are relatively low (<2%) and generally comparable (slightly larger for the 2nd FA mode). The angles evolution of the 2nd FA/SS modes is shown in Figure 55. The definition of the angles of the 2nd FA/SS modes is similar to that of 1st FA/SS modes and is illustrated in Figure 16 (b). The angles of the 2nd FA mode are roughly 0°, and those of 2nd SS mode are close to 270°, confirming that they are perpendicular. Two animation videos of the mode shape evolution of the 2nd FA/SS modes on July 6 are made and included in the supplementary files.

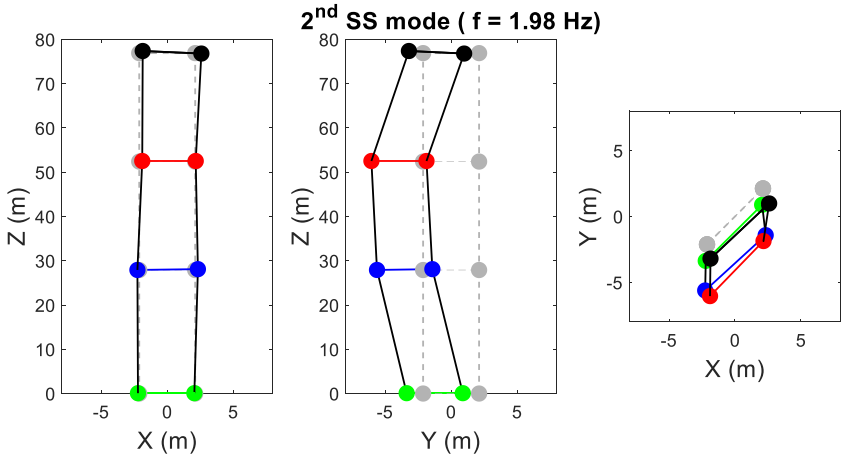

Figure 49. Identified 2nd SS mode at 8:31 on July 6.

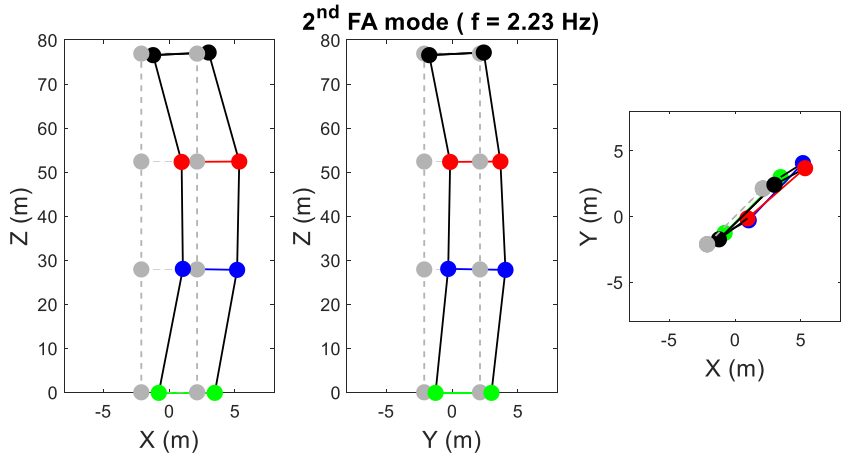

Figure 50. Identified 2nd FA mode at 8:31 on July 6.

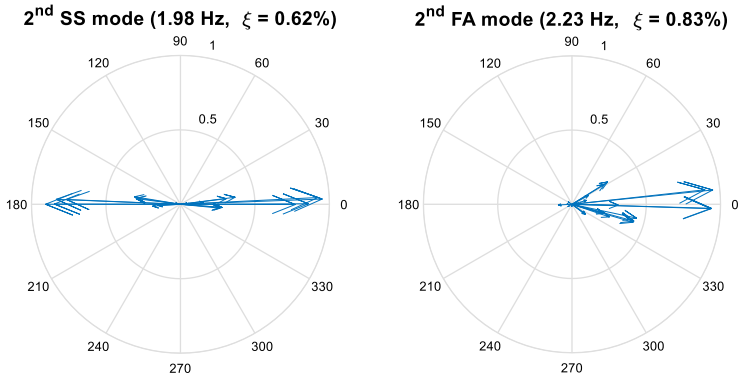

Figure 51. Compass plot of 2nd SS/FA modes at 8:31 on July 6.

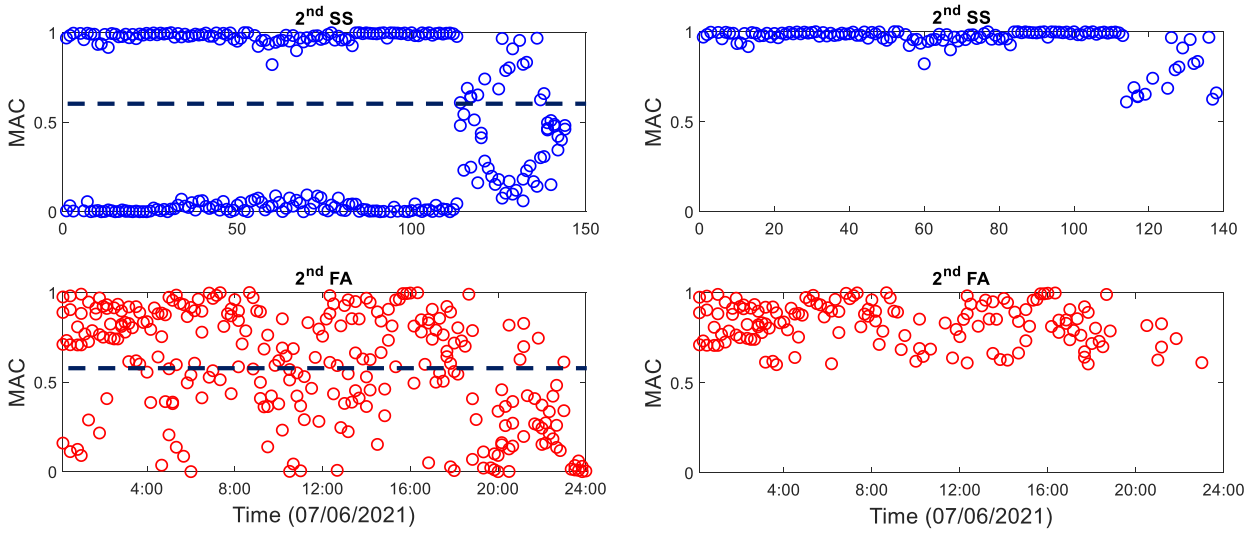

(a) (b)

Figure 52. (a) MAC values evolution with reference SS/FA modes on July 6; (b) SS/FA modes are selected based on MAC values larger than 0.6.

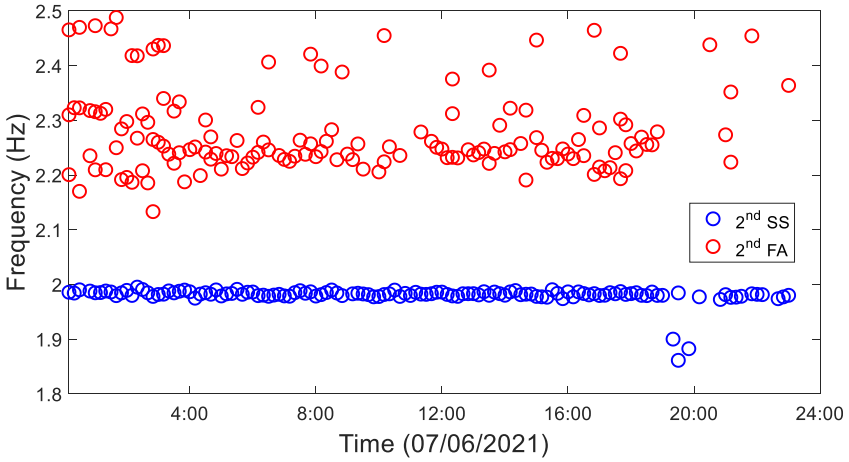

Figure 53. Frequencies evolution of identified 2nd FA/SS modes on July 6.

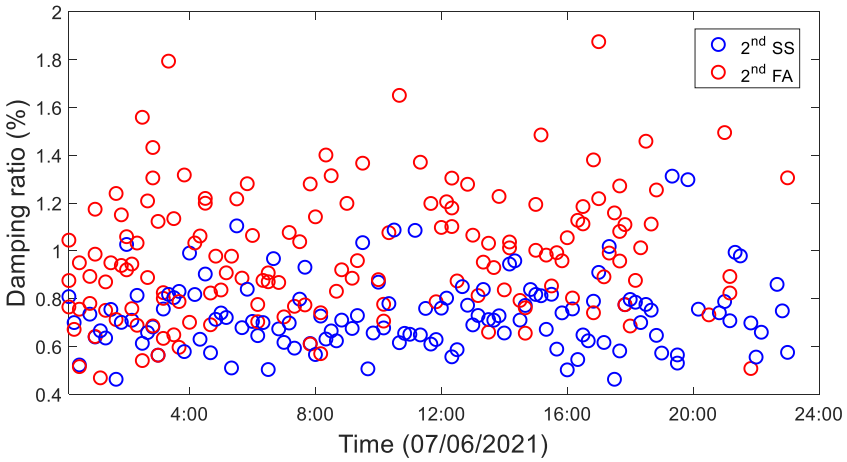

Figure 54. Damping ratios evolution of identified 2nd FA/SS modes on July 6.

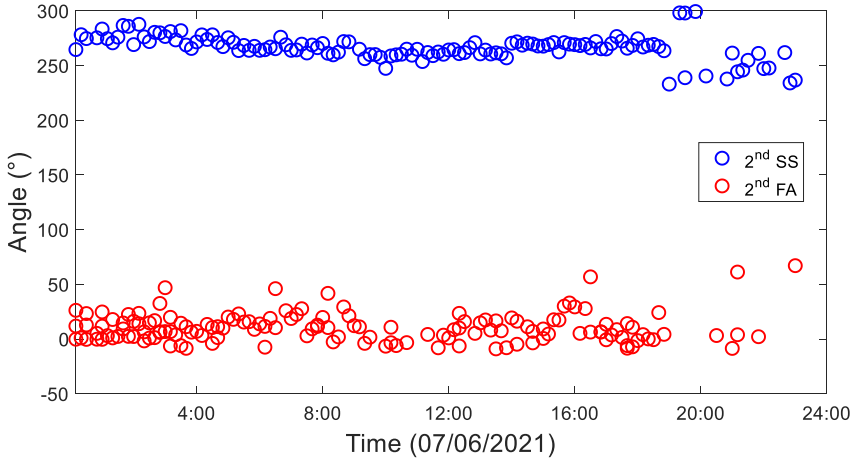

Figure 55. Evolution of angles of 2nd FA/SS modes on July 6.

5.5 System identification over one week with varying rotating speed (4/21 – 4/27)

The system identification results using one week of data (April 21 – April 27) are shown in Figure 56. It is seen that the identified 3P, 6P, and 9P are consistent with SCADA even for some rapidly varying situations. The 2nd FA/SS modes are not reliably identified in this week due to the interference of blades and 12P frequencies. The FA/SS modes are separated based on the similar strategy using the MAC values with the reference modes (9:17 on April 22). To improve the classification, the FA/SS modes are first transformed to the FA-SS coordinate based on SCADA. The classification process is shown in Figure 57, where the circles below the line $y = x - 0.3$ are classified as the FA mode, and the circles above the line $y = x + 0.3$ are classified as the SS mode.

The evolution of the identified natural frequencies, MAC values, and damping ratios from 4/21 to 4/27 are shown in Figure 58, Figure 59 and Figure 60, respectively. Similar to the observations made on April 22 and 25, the frequencies of SS mode generally stay constant while those of FA mode show evident variability. Most of the MAC values are close to one. The

damping ratios of SS mode are low and stable, while those of FA mode are significantly larger with higher standard deviation due to aerodynamic damping. The statistics (including mean, standard deviations (std), minimum and maximum values) of natural frequencies, MAC values and damping ratios are reported in Table 2, Table 3 and Table 4, respectively. It is observed that, the mean frequencies of FA/SS modes across different days are very close, and those of the SS mode is consistently smaller than the FA mode. The standard deviations on 4/25 and 4/27 are larger than other days due to the varying rotating speed. The mean MAC values are generally larger than 0.95 in every day of the week which verifies the system identification accuracy. The mean damping ratios of the FA mode in every day are consistently larger than those of the SS mode, and also have larger standard deviations.

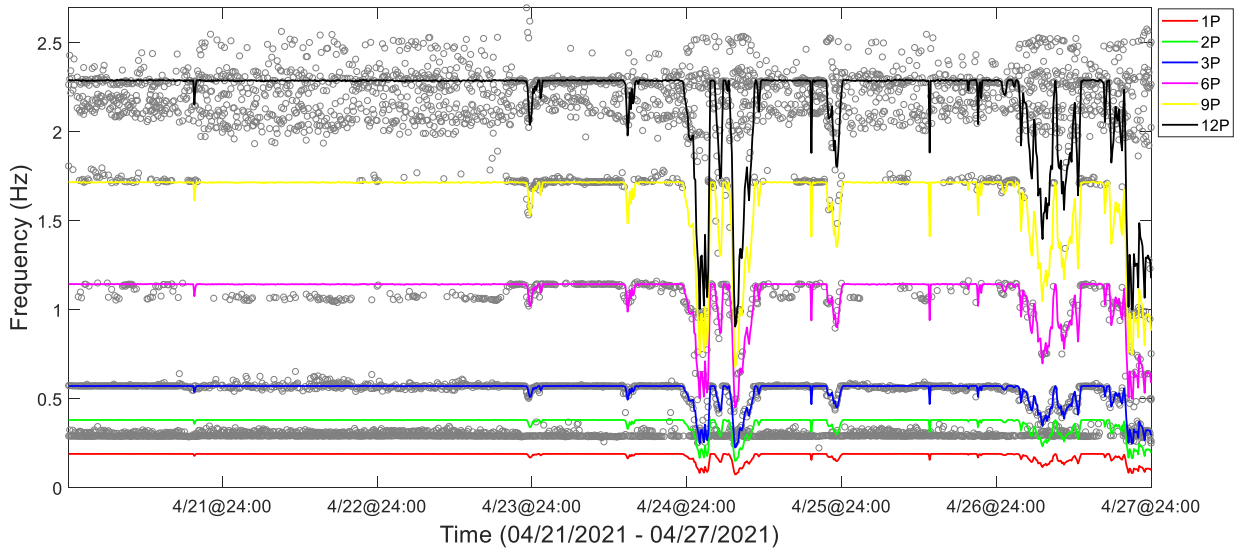

Figure 56. Automated system identification results from 4/21 to 4/27.

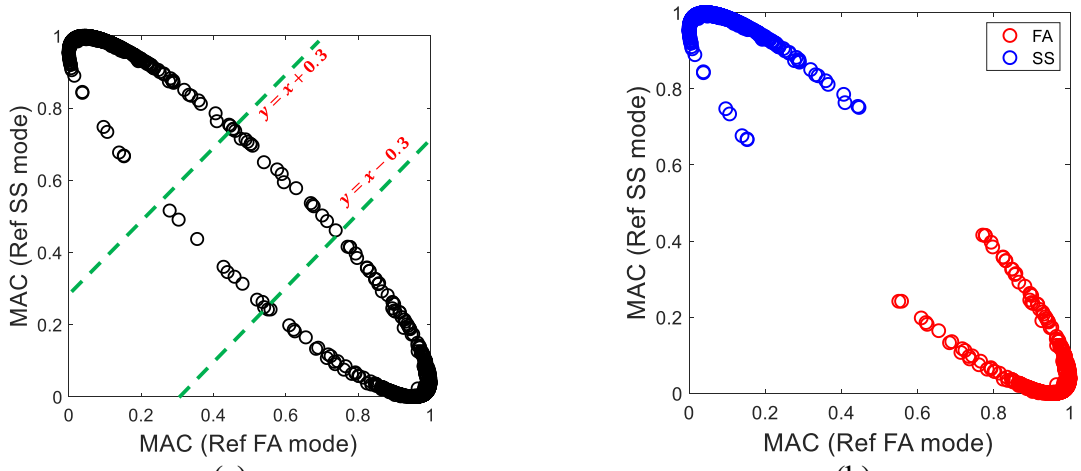

(a) (b)

Figure 57. (a) MAC values with reference FA mode versus that with reference SS mode from 4/21 to 4/27; (b) Separation results.

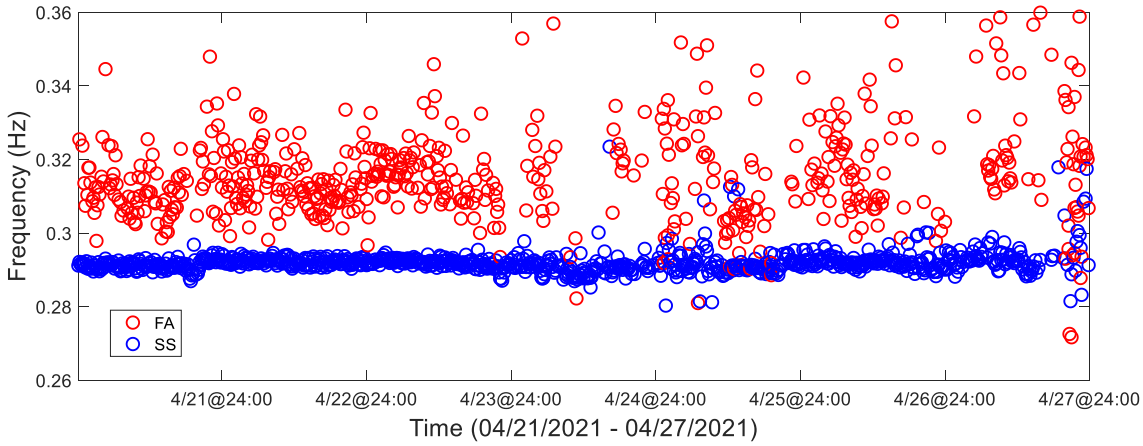

Figure 58. Frequencies evolution of identified FA/SS modes from 4/21 to 4/27.

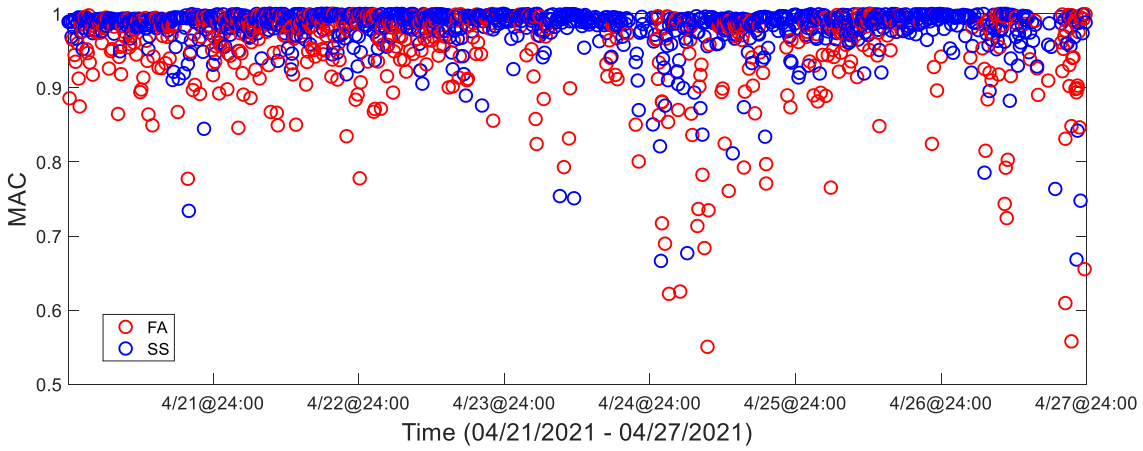

Figure 59. MAC evolution of identified FA/SS modes from 4/21 to 4/27.

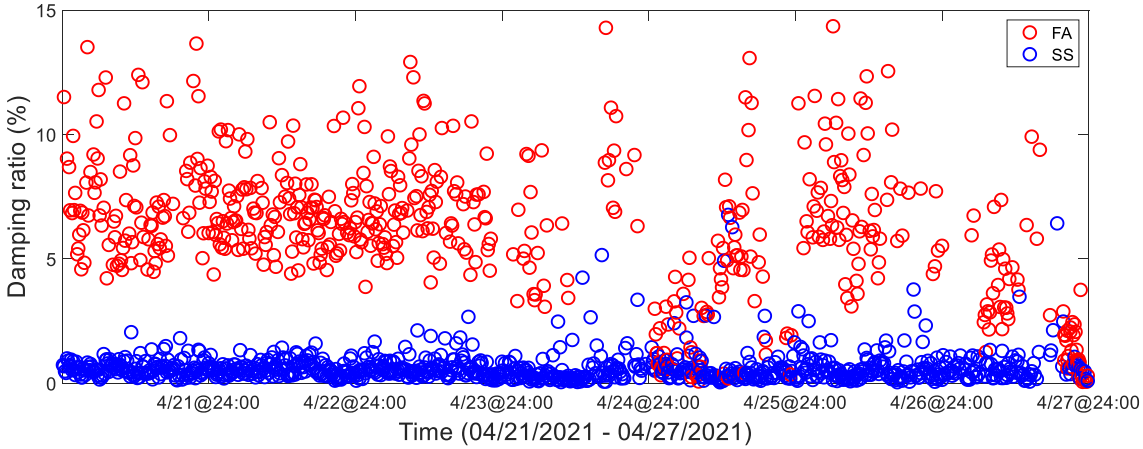

Figure 60. Damping ratios evolution of identified FA/SS modes from 4/21 to 4/27.

Table 2. Statistics of natural frequencies of identified FA/SS modes from 4/21 to 4/27.

		Mean	Std	Min	Max
4/21	FA	0.313	0.009	0.298	0.348
	SS	0.291	0.001	0.289	0.295
4/22	FA	0.313	0.007	0.298	0.338
	SS	0.292	0.001	0.290	0.294
4/23	FA	0.316	0.008	0.293	0.346
	SS	0.292	0.001	0.288	0.295
4/24	FA	0.317	0.013	0.282	0.353
	SS	0.291	0.002	0.288	0.296
4/25	FA	0.313	0.015	0.281	0.352
	SS	0.293	0.005	0.289	0.313
4/26	FA	0.317	0.012	0.298	0.358
	SS	0.292	0.001	0.288	0.296
4/27	FA	0.323	0.018	0.272	0.360
	SS	0.295	0.006	0.283	0.317
All	FA	0.315	0.011	0.272	0.360
	SS	0.292	0.003	0.283	0.317

Table 3. Statistics of MAC values of identified FA/SS modes from 4/21 to 4/27.

		Mean	Std	Min	Max
4/21	FA	0.96	0.04	0.78	1.00
	SS	0.98	0.02	0.84	1.00
4/22	FA	0.96	0.04	0.83	1.00
	SS	0.98	0.02	0.92	1.00
4/23	FA	0.96	0.04	0.78	1.00
	SS	0.99	0.02	0.89	1.00
4/24	FA	0.93	0.06	0.79	1.00
	SS	0.99	0.02	0.87	1.00
4/25	FA	0.91	0.11	0.55	1.00
	SS	0.97	0.05	0.67	1.00
4/26	FA	0.96	0.04	0.77	1.00
	SS	0.99	0.01	0.91	1.00
4/27	FA	0.95	0.07	0.72	1.00
	SS	0.96	0.07	0.67	1.00
All	FA	0.95	0.06	0.55	1.00
	SS	0.98	0.03	0.67	1.00

Table 4. Statistics of damping ratios (%) of identified FA/SS modes from 4/21 to 4/27.

		Mean	Std	Min	Max
4/21	FA	7.4	2.2	4.2	13.7
	SS	0.6	0.3	0.2	2.1

4/22	FA	6.9	1.5	4.4	10.7
	SS	0.6	0.3	0.1	1.6
4/23	FA	7.2	1.9	3.9	12.9
	SS	0.6	0.4	0.1	2.1
4/24	FA	6.9	2.7	3.3	14.3
	SS	0.5	0.6	0.1	3.4
4/25	FA	4.1	2.9	0.1	13.1
	SS	0.6	1.0	0.0	6.8
4/26	FA	7.3	2.4	3.1	14.4
	SS	0.5	0.4	0.0	2.9
4/27	FA	3.7	2.6	0.1	13.5
	SS	0.6	0.4	0.1	2.5
All	FA	6.5	2.6	0.1	14.4
	SS	0.6	0.5	0.0	6.8

5.6 System identification over one week with parked turbine (7/5 – 7/11)

5.6.1 Identification of 1st FA/SS modes

To investigate the performance of automated system identification on both 1st and 2nd FA/SS modes when the turbine is parked, one week of data from July 5 to July 11 is used, and the results are shown in Figure 61. It is observed that both 1st and 2nd FA/SS modes are consistently identified across this week. The 1st FA/SS modes are separated using the similar strategy based on MAC values with the reference modes (8:31 on July 6), and then the circles below the line $y = x - 0.3$ are classified as the FA mode, and the circles above the line $y = x + 0.3$ are classified as the SS mode.

The evolution of the identified natural frequencies, MAC values, and damping ratios from 7/5 to 7/11 are shown in Figure 62, Figure 63 and Figure 64, respectively. Similar to the observations made on July 6, the frequencies of FA/SS modes are close and show similar level of variability. The frequency of the FA mode in parked condition is smaller than that when turbine is in operation (0.29 Hz versus 0.31 Hz), probably due to the absence of aerodynamics. The damping ratios of the FA mode in parked condition are slightly larger but generally comparable to those of the SS mode (generally < 2%), but are significantly smaller than that when the turbine is in operation (4 - 10%) due to the absence of aerodynamic damping. The overall statistics of modal parameters of the FA/SS modes from 7/5 to 7/11 are reported in Table 5.

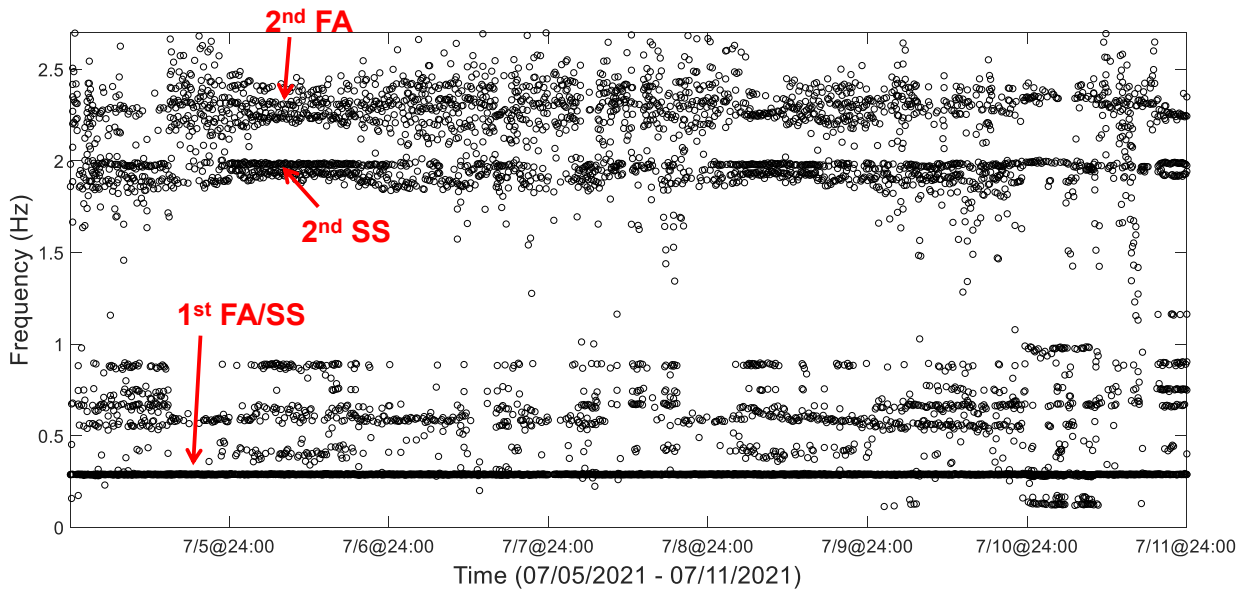

Figure 61. Automated system identification results from 7/5 to 7/11.

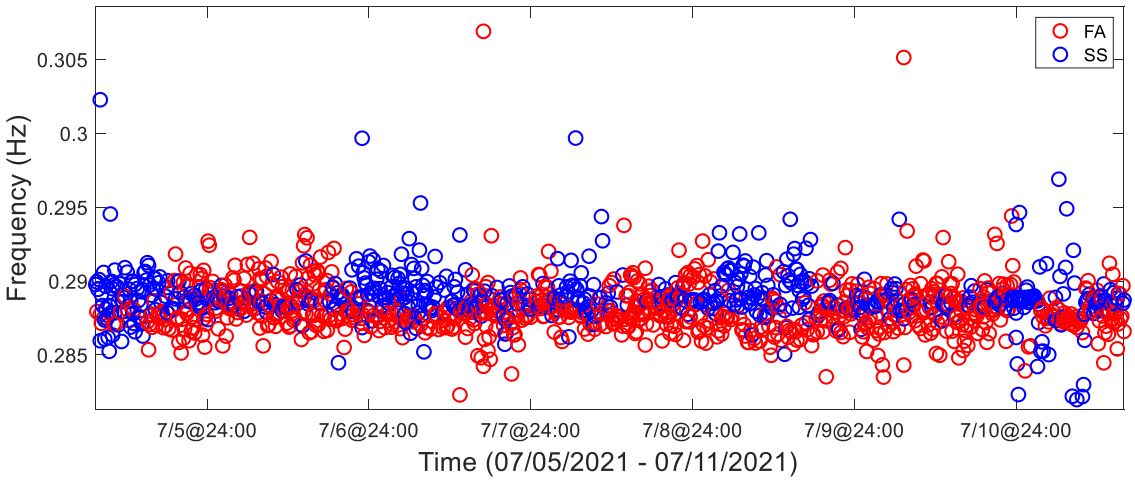

Figure 62. Frequencies evolution of identified FA/SS modes from 7/5 to 7/11.

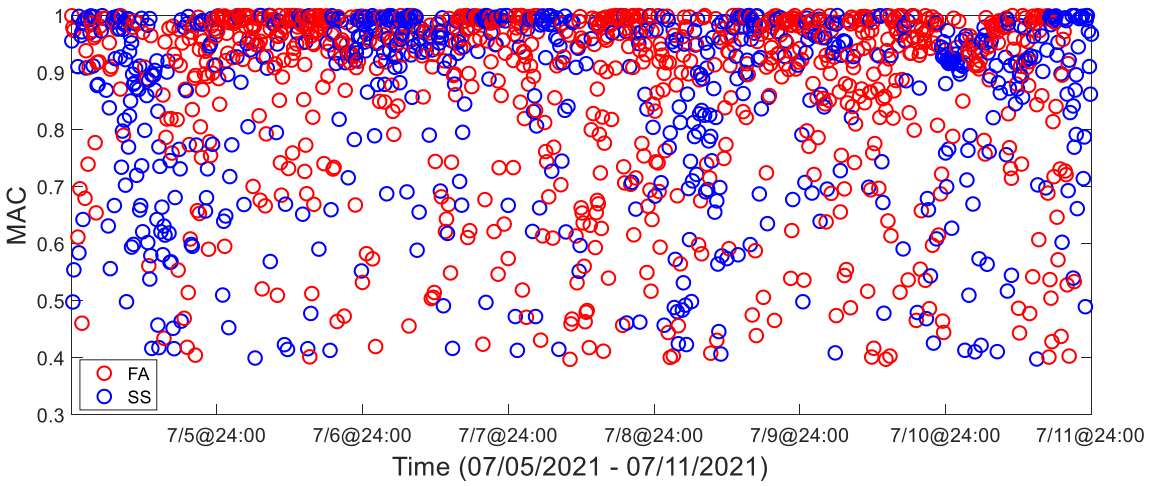

Figure 63. MAC evolution of identified FA/SS modes from 7/5 to 7/11.

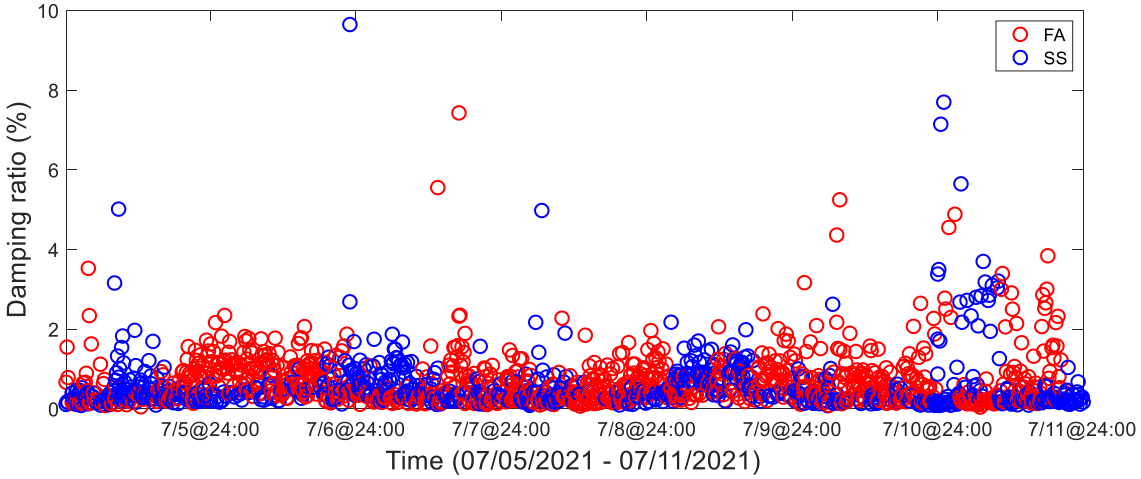

Figure 64. Damping ratios evolution of identified FA/SS modes from 7/5 to 7/11.

Table 5. Statistics of modal parameters of identified FA/SS modes from 7/5 to 7/11.

		Mean	Std	Min	Max
Frequency	FA	0.288	0.002	0.280	0.296
	SS	0.289	0.002	0.280	0.300
MAC	FA	0.86	0.17	0.40	1.00
	SS	0.85	0.17	0.40	1.00
Damping ratio (%)	FA	0.8	0.8	0.0	5.6
	SS	0.6	0.7	0.1	5.6

5.6.2 Identification of 2nd FA/SS modes

The evolution of natural frequencies, MAC values, and damping ratios of the identified 2nd FA/SS modes are shown in Figure 65, Figure 66 and Figure 67, respectively. A similar strategy based on MAC values with the reference modes (at 8:31 on July 6) are used to select the physical

modes (MAC > 0.6) and remove spurious modes. It is seen that the frequencies of the 2nd SS mode generally stay stable while those of the 2nd FA mode have larger variation. The MAC values of both 2nd FA/SS modes show significant variability, probably due to noise and identification errors. The damping ratios of both 2nd FA/SS modes are low (generally < 2%) and comparable (slightly larger for the 2nd FA mode). The angles evolution of the 2nd FA/SS modes is shown in Figure 68. The 2nd FA and SS modes stay perpendicular over time. The statistics (mean, standard deviation, minimum and maximum values) of natural frequencies, MAC values and damping ratios of the 2nd FA/SS modes are reported in Table 6, Table 7 and Table 8, respectively.

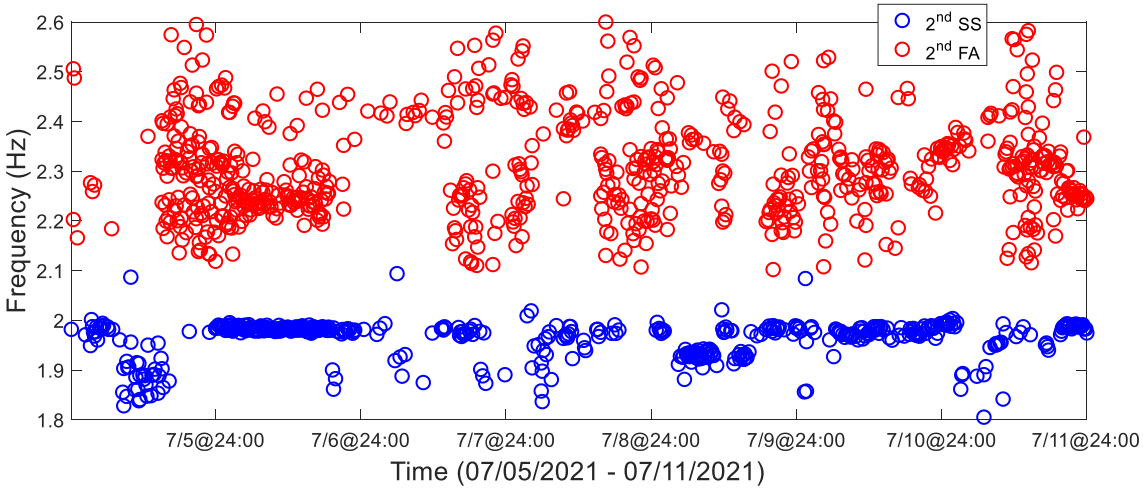

Figure 65. Frequencies evolution of identified 2nd FA/SS modes from 7/5 to 7/11.

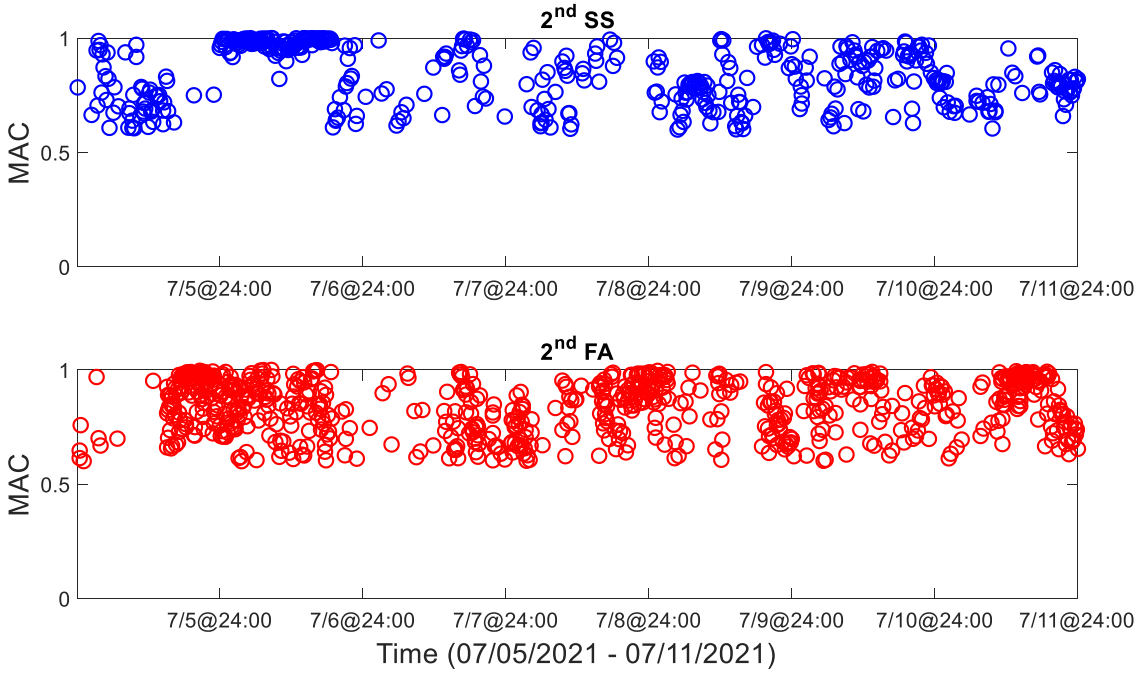

Figure 66. MAC evolution of identified 2nd FA/SS modes from 7/5 to 7/11.

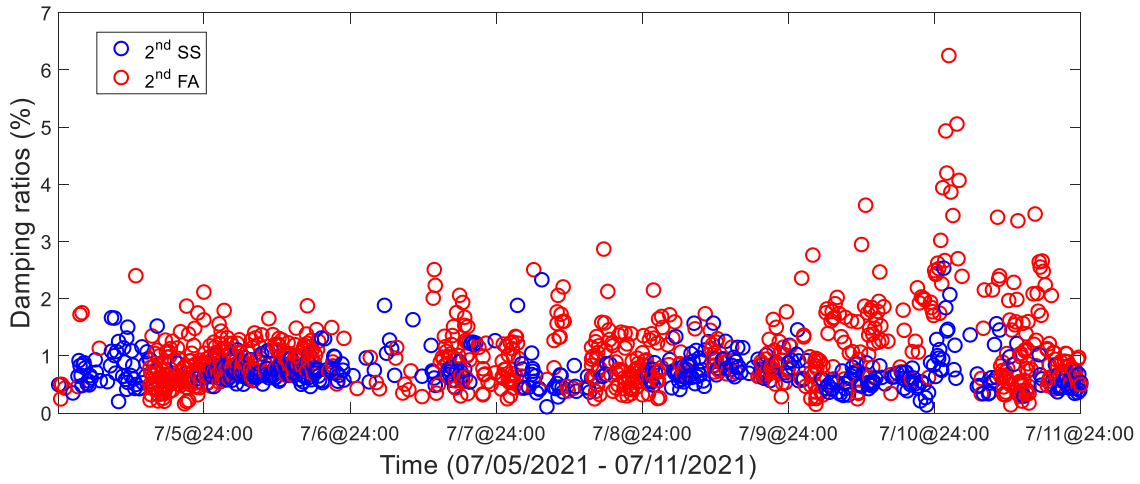

Figure 67. Damping ratios evolution of identified 2nd FA/SS modes from 7/5 to 7/11.

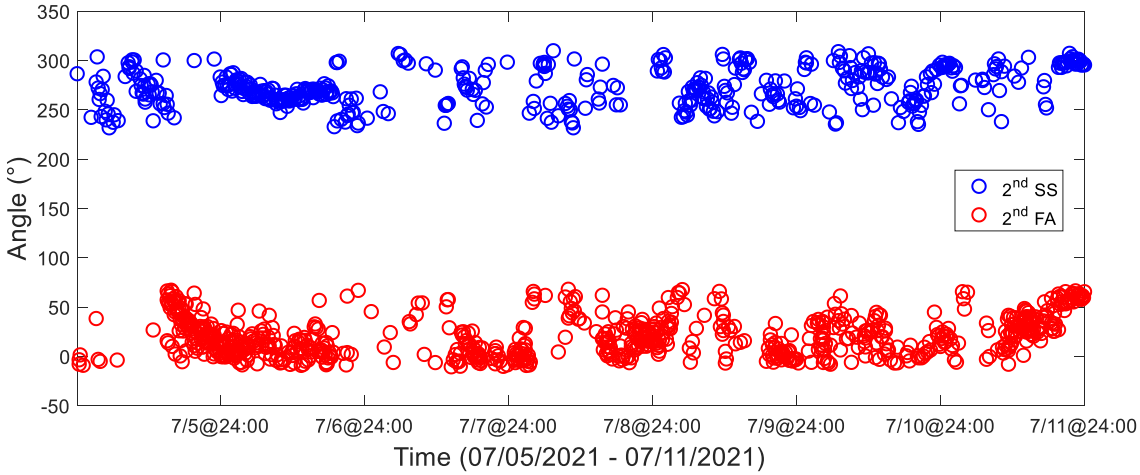

Figure 68. Evolution of angles of 2nd FA/SS modes from 7/5 to 7/11.

Table 6. Statistics of natural frequencies of identified 2nd FA/SS modes from 7/5 to 7/11.

		Mean	Std	Min	Max
7/5	2nd SS	1.944	0.045	1.865	1.987
	2nd FA	2.242	0.079	2.119	2.370
7/6	2nd SS	1.983	0.004	1.974	1.995
	2nd FA	2.243	0.046	2.133	2.467
7/7	2nd SS	1.973	0.022	1.891	1.990
	2nd FA	2.285	0.091	2.118	2.448
7/8	2nd SS	1.972	0.029	1.904	2.019
	2nd FA	2.340	0.073	2.244	2.459
7/9	2nd SS	1.963	0.030	1.912	2.021
	2nd FA	2.280	0.084	2.102	2.466
7/10	2nd SS	1.977	0.011	1.927	1.993
	2nd FA	2.293	0.050	2.121	2.401

7/11	2nd SS	1.983	0.015	1.940	2.004
	2nd FA	2.285	0.048	2.188	2.412
All	2nd SS	1.977	0.021	1.865	2.021
	2nd FA	2.271	0.065	2.102	2.467

Table 7. Statistics of MAC values of identified 2nd FA/SS modes from 7/5 to 7/11.

		Mean	**Std**	**Min**	**Max**
7/5	2nd SS	0.81	0.14	0.63	0.99
	2nd FA	0.81	0.13	0.66	0.97
7/6	2nd SS	0.97	0.04	0.66	1.00
	2nd FA	0.86	0.10	0.61	1.00
7/7	2nd SS	0.91	0.10	0.66	1.00
	2nd FA	0.85	0.13	0.61	0.99
7/8	2nd SS	0.79	0.11	0.60	0.94
	2nd FA	0.83	0.12	0.60	0.99
7/9	2nd SS	0.85	0.12	0.60	1.00
	2nd FA	0.83	0.11	0.67	1.00
7/10	2nd SS	0.85	0.11	0.61	0.99
	2nd FA	0.90	0.10	0.68	0.99
7/11	2nd SS	0.80	0.05	0.66	0.95
	2nd FA	0.81	0.10	0.63	0.98
All	2nd SS	0.89	0.11	0.60	1.00
	2nd FA	0.85	0.11	0.60	1.00

Table 8. Statistics of damping ratios (%) of identified 2nd FA/SS modes from 7/5 to 7/11.

		Mean	**Std**	**Min**	**Max**
7/5	2nd SS	0.8	0.3	0.5	1.5
	2nd FA	1.3	0.7	0.5	2.4
7/6	2nd SS	0.7	0.1	0.5	1.1
	2nd FA	1.0	0.2	0.5	1.8
7/7	2nd SS	0.7	0.2	0.5	1.3
	2nd FA	1.3	0.6	0.3	2.5
7/8	2nd SS	0.6	0.4	0.1	1.9
	2nd FA	1.3	0.6	0.4	2.5
7/9	2nd SS	0.8	0.2	0.4	1.6
	2nd FA	1.0	0.4	0.5	2.2
7/10	2nd SS	0.6	0.1	0.4	0.9
	2nd FA	1.5	0.5	0.6	2.9
7/11	2nd SS	0.7	0.3	0.3	1.8
	2nd FA	1.5	1.1	0.4	4.9
All	2nd SS	0.7	0.2	0.1	1.9

	2nd FA	1.2	0.6	0.3	4.9

5.7 System identification over a 3-month period (4/19 – 7/19)

To verify the capability and accuracy of the proposed automated system identification algorithm for long time monitoring, three months of data (from April 19 to July 19) have been used to identify the modal parameters of B2 wind turbine. The automated system identification results are shown in Figure 69. There are some gaps/empty spaces in the figure, from April 30 to May 2, May 11 to May 17, as well as June 17. These datasets are missing due to automatic restart of the data acquisition PC at the turbine. This issue has been resolved and data has been streaming since then. Table 9 and Table 10 provide the statistical properties of the natural frequencies, damping ratios, and MAC values with reference modes (9:17 on April 22 for 1st FA/SS modes, and 8:31 on July 6 for 2nd FA/SS modes) over 11,097 datasets collected in this period. In Table 10, the datasets from 6/19 to 7/19 are used to represent the statistics of the 2nd FA/SS modes since the second bending modes are not reliably identified outside this time window. It is seen that the frequencies of the 1st FA and SS modes generally stay constant over this long period of time with very small standard deviations. The damping ratios of the FA mode are higher and have larger variability than those of the SS mode. The 2nd FA mode has larger standard deviation of frequencies and higher damping ratio than the 2nd SS mode.

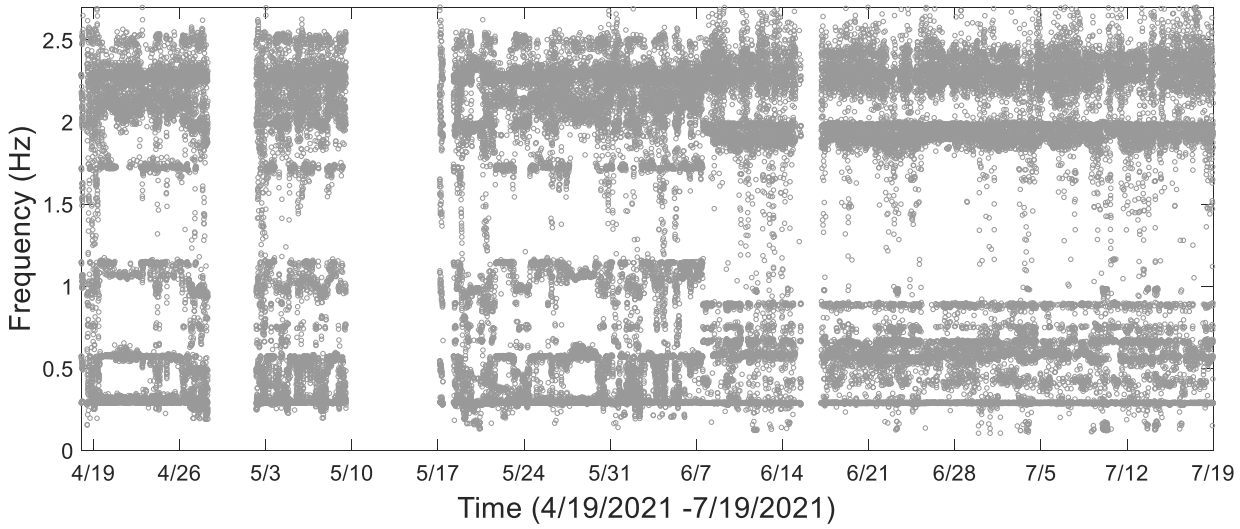

Figure 69. Automated system identification results from 4/19 to 7/19.

Table 9. Statistics of modal parameters of identified FA/SS modes from 4/19 to 7/19.

		Mean	Std	Min	Max
Frequency	FA	0.294	0.014	0.270	0.360
	SS	0.294	0.012	0.270	0.360
MAC	FA	0.89	0.10	0.55	1.00
	SS	0.88	0.11	0.55	1.00
Damping ratio (%)	FA	1.5	2.2	0.0	14.6
	SS	1.3	2.1	0.0	14.3

Table 10. Statistics of modal parameters of identified 2nd FA/SS modes from 6/19 to 7/19.

		Mean	Std	Min	Max
Frequency	2nd SS	1.978	0.021	1.835	2.080
	2nd FA	2.273	0.072	2.102	2.598
MAC	2nd SS	0.90	0.10	0.60	1.00
	2nd FA	0.84	0.11	0.60	1.00
Damping ratio (%)	2nd SS	0.7	0.2	0.1	2.9
	2nd FA	1.2	0.5	0.2	4.9

6. Conclusions

In this report, an automated system identification approach is formulated and implemented to automatically extract modal parameters of B2 offshore wind turbine in BIWF using the SSI-DATA method. An introduction of system identification methods is first presented, and then a brief review of the SSI-DATA method is included. An automation procedure for judging stable modes and selecting the best system order is proposed based on the relative change of natural frequencies, MAC values, and damping ratios over consecutive orders of the state-space model. An overview of the continuous monitoring system is also included. The proposed automated system identification algorithm is capable of identifying the 1st FA/SS modes of the B2 wind turbine when the turbine is in operation, and both the 1st and 2nd FA/SS modes when the turbine is parked, as well as estimating 3P and 6P as stable dynamics without the need for interference of a human operator.

The automated system identification algorithm is implemented for different periods of time and environmental conditions: (1) a full day analysis under different turbine conditions, including constant rotor speed, rapidly varying rotor speed, and parked turbine. (2)Two cases of a full week analysis, one is from 4/21 to 4/27 when turbine is in operation, and the other one is from 7/5 to 7/11 with parked turbine. (3) An automated analysis over a 3-month period from April 19 to July 19. After reviewing the identification results, the following conclusions are made:

(I) The FA/SS modes have closely spaced natural frequencies and can be separated based on MAC values of mode shapes (ideally in FA-SS coordinates). Mode shapes of the FA/SS modes are affected by the yaw angle and change with time.

(II) When wind conditions are stable and the yaw angle does not change drastically, as in April 22, the FA/SS modes can be separated perfectly based on the MAC values. However, for rapidly varying wind conditions, some classification errors are observed due to the effects of yaw angle, as well as the effects of 3P. The classification accuracy can be improved when the FA/SS modes are transformed from the global coordinate to the FA-SS coordinate.

(III) The natural frequencies of the SS mode are constant over time and have very small variation, but those of FA mode have larger variability. The SS mode has low and constant

damping ratios, but the FA mode has larger damping with larger variability due to the effects of aerodynamics.

(IV) The 3P and 6P are evident from the data and consistently estimated over different datasets. The identified 3P and 6P from the data are highly consistent with SCADA. The response amplitude is magnified when the 3P frequency gets close to the natural frequencies of the FA/SS modes due to modal resonance.

(V) The 2nd FA/SS modes can only be identified with reasonable accuracy when the turbine is parked, i.e., the interference from 12P and modes of blades are not present. The 2nd FA/SS modes have different natural frequencies and can be easily separated based on frequency, but spurious modes are present from identification results and can be removed based on MAC values.

(VI) Similar to the FA/SS modes, the frequencies of the 2nd SS mode are constant over time and have very small variation, but those of FA mode have larger variability. The 2nd FA mode has higher damping with larger variability than the 2nd SS mode due to the effect of aerodynamics.

(VII) The system identification results under two cases of a full week analysis, as well as using three months of data verify the effectiveness, efficiency, and robustness of the proposed algorithm for long-term monitoring of this offshore wind turbine.

Acknowledgments

This is study has been completed as part of the Bureau of Safety and Environmental Enforcement (BSEE) project “Block Island wind farm structural monitoring project” under contract number 140E0119C0003. Additional support for this study has been provided by Massachusetts Clean Energy Center under the AmplifyMass program. The team is grateful to the help and support of GE Renewable Energy personnel including Jody Grainger, Trent Pack, Michael Hanson, and Shane Watts as well as Orsted personnel including Steven Wilkey, Jorge Ramirez Basurto, Bryan Wilson, and Robert Gilpin and for their help with installation of the monitoring system and access to the turbine SCADA data. The opinions, findings, and conclusions expressed in this document are those of the authors and do not necessarily represent the views of the sponsors and organizations involved in this project.

References

1. Van Overschee, P. and B. De Moor, *Subspace identification for linear systems: Theory—Implementation—Applications*. 2012: Springer Science & Business Media.
2. Peeters, B., *System identification and damage detection in civil engeneering.* 2000.
3. Friswell, M. and J.E. Mottershead, *Finite element model updating in structural dynamics*. Vol. 38. 2013: Springer Science & Business Media.
4. Brownjohn, J.M.W., P. Moyo, P. Omenzetter, and Y. Lu, *Assessment of highway bridge upgrading by dynamic testing and finite-element model updating.* Journal of Bridge Engineering, 2003. **8**(3): p. 162-172.
5. Zhang, Q., T.-Y.P. Chang, and C.C. Chang, *Finite-element model updating for the Kap Shui Mun cable-stayed bridge.* Journal of Bridge Engineering, 2001. **6**(4): p. 285-293.

6. Teughels, A. and G. De Roeck, *Structural damage identification of the highway bridge Z24 by FE model updating.* Journal of Sound and Vibration, 2004. **278**(3): p. 589-610.
7. Reynders, E., G.D. Roeck, P. Gundes Bakir, and C. Sauvage, *Damage identification on the Tilff Bridge by vibration monitoring using optical fiber strain sensors.* Journal of engineering mechanics, 2007. **133**(2): p. 185-193.
8. Moaveni, B., A. Stavridis, G. Lombaert, J.P. Conte, and P.B. Shing, *Finite-element model updating for assessment of progressive damage in a 3-story infilled RC frame.* Journal of Structural Engineering, 2012. **139**(10): p. 1665-1674.
9. Song, M., S. Yousefianmoghadam, M.-E. Mohammadi, B. Moaveni, A. Stavridis, and R.L. Wood, *An application of finite element model updating for damage assessment of a two-story reinforced concrete building and comparison with lidar.* Structural Health Monitoring, 2018. **17**(5): p. 1129-1150.
10. Behmanesh, I. and B. Moaveni, *Probabilistic identification of simulated damage on the Dowling Hall footbridge through Bayesian finite element model updating.* Structural Control and Health Monitoring, 2015. **22**(3): p. 463-483.
11. Lam, H.-F., J. Yang, and S.-K. Au, *Bayesian model updating of a coupled-slab system using field test data utilizing an enhanced Markov chain Monte Carlo simulation algorithm.* Engineering Structures, 2015. **102**: p. 144-155.
12. Song, M., B. Moaveni, C. Papadimitriou, and A. Stavridis, *Accounting for amplitude of excitation in model updating through a hierarchical Bayesian approach: Application to a two-story reinforced concrete building.* Mechanical Systems and Signal Processing, 2019. **123**: p. 68-83.
13. Song, M., I. Behmanesh, B. Moaveni, and C. Papadimitriou, *Accounting for Modeling Errors and Inherent Structural Variability through a Hierarchical Bayesian Model Updating Approach: An Overview.* Sensors, 2020. **20**(14): p. 3874.
14. Chopra, A.K. and A.K. Chopra, *Dynamics of structures: theory and applications to earthquake engineering*. Vol. 3. 2007: Pearson/Prentice Hall Upper Saddle River, NJ.
15. De Callafon, R.A., B. Moaveni, J.P. Conte, X. He, and E. Udd, *General realization algorithm for modal identification of linear dynamic systems.* Journal of engineering mechanics, 2008. **134**(9): p. 712-722.
16. Juang, J.-N. and R.S. Pappa, *An eigensystem realization algorithm for modal parameter identification and model reduction.* Journal of guidance, control, and dynamics, 1985. **8**(5): p. 620-627.
17. James, G., T.G. Carne, and J.P. Lauffer, *The natural excitation technique (NExT) for modal parameter extraction from operating structures.* Modal Analysis-the International Journal of Analytical and Experimental Modal Analysis, 1995. **10**(4): p. 260.
18. Brincker, R., L. Zhang, and P. Andersen. *Modal identification from ambient responses using frequency domain decomposition*. in *Proc. of the 18*'International Modal Analysis Conference (IMAC), San Antonio, Texas*. 2000.
19. Peeters, B. and G. De Roeck, *Reference-based stochastic subspace identification for output-only modal analysis.* Mechanical systems and signal processing, 1999. **13**(6): p. 855-878.
20. Moser, P., *Continuous monitoring of the Dowling Hall Footbridge*. 2010, Tufts University.